remote sensing

MDPI

Article

Trend Analysis of High-Resolution Soil Moisture Data Based on GAN in the Three-River-Source Region During the 21st Century

Zhuoqun Li [1,2], Siqiong Luo [1,*], Xiaoqing Tan [1,2] and Jingyuan Wang [1]

[1] Key Laboratory of Cryospheric Science and Frozen Soil Engineering, Northwest Institute of Eco-Environment and Resources, Chinese Academy of Sciences, Lanzhou 730000, China; lizhuoqun221@mails.ucas.ac.cn (Z.L.); tanxiaoqing@nieer.ac.cn (X.T.); wangjingyuan@lzb.ac.cn (J.W.)
[2] University of Chinese Academy of Sciences, Beijing 100049, China
* Correspondence: lsq@lzb.ac.cn

Abstract: Soil moisture (SM) is a crucial factor in land-atmosphere interactions and climate systems, affecting surface energy, water budgets, and weather extremes. In the Three-River-Source Region (TRSR) of China, rapid climate change necessitates precise SM monitoring. This study employs a novel UNet-Gan model to integrate and downscale SM data from 17 CMIP6 models, producing a high-resolution (0.1°) dataset called $CMIP6_{UNet\text{-}Gan}$. This dataset includes SM data for five depth layers (0–10 cm, 10–30 cm, 30–50 cm, 50–80 cm, 80–110 cm), four Shared Socioeconomic Pathways (SSP1-2.6, SSP2-4.5, SSP3-7.0, SSP5-8.5). The UNet-Gan model demonstrates strong performance in data fusion and downscaling, especially in shallow soil layers. Analysis of the $CMIP6_{UNet\text{-}Gan}$ dataset reveals an overall increasing trend in SM across all layers, with higher rates under more intense emission scenarios. Spatially, moisture increases vary, with significant trends in the western Yangtze and northeastern Yellow River regions. Deeper soils show a slower response to climate change, and seasonal variations indicate that moisture increases are most pronounced in spring and winter, followed by autumn, with the least increase observed in summer. Future projections suggest higher moisture increase rates in the early and late 21st century compared to the mid-century. By the end of this century (2071–2100), compared to the Historical period (1995–2014), the increase in SM across the five depth layers ranges from: 5.5% to 11.5%, 4.6% to 9.2%, 4.3% to 7.5%, 4.5% to 7.5%, and 3.3% to 6.5%, respectively.

Keywords: soil moisture; statistical downscaling; CMIP6; Generative Adversarial Network; deep learning; Three-River-Source Region

Citation: Li, Z.; Luo, S.; Tan, X.; Wang, J. Trend Analysis of High-Resolution Soil Moisture Data Based on GAN in the Three-River-Source Region During the 21st Century. *Remote Sens.* **2024**, *16*, 4367. https://doi.org/10.3390/rs16234367

Academic Editor: Gabriel Senay

Received: 30 August 2024
Revised: 14 November 2024
Accepted: 19 November 2024
Published: 22 November 2024

1. Introduction

Soil moisture (SM) is a critical variable in the land-atmosphere interactions and plays a vital role in various aspects of the Earth's climate system. It influences surface energy and water budgets, including sensible and latent heat fluxes, radiation exchange, and vegetation growth [1]. SM affects local and regional climate patterns by modulating evaporation and precipitation processes, contributing significantly to weather extremes and long-term climate behavior [2,3]. Given its central role in climate dynamics, understanding and predicting SM variations is essential for managing water resources, agricultural productivity, and responding to climate-related challenges [4,5].

The Three-River-Source Region (TRSR) in China, located at the headwaters of the Yangtze, Yellow, and Lancang rivers, is particularly sensitive to climate change [6,7]. The region experiences warming at rates more than twice the global average and has witnessed significant increases in precipitation since the early 21st century [8,9]. This accelerated warming and altered precipitation patterns have profound effects on soil temperatures, permafrost stability, and freeze-thaw processes in the TRSR [10,11]. Accurate monitoring and modeling of SM in this region are crucial for understanding its climate impacts and for developing effective adaptation strategies to mitigate adverse effects.

Recent advancements in climate modeling, particularly the Coupled Model Intercomparison Project Phase 6 (CMIP6), provide valuable tools for predicting future SM conditions under various emission scenarios [12,13]. CMIP6 offers a suite of climate models and scenarios, including the Shared Socioeconomic Pathways (SSP), which represent diverse pathways of future socio-economic and environmental development [14]. Evaluating future SM projections from CMIP6 models is essential for anticipating changes in drought characteristics, heatwave patterns, and overall water availability, which are critical for planning and implementing climate adaptation strategies [15,16].

High-resolution CMIP6 data are crucial for understanding and predicting localized climate impacts, such as extreme events and changes in agricultural productivity. However, CMIP6 models typically produce data at relatively coarse spatial resolutions, limiting their ability to capture fine-scale variations in climate variables. To address this limitation, various statistical downscaling methods have been developed to enhance the spatial resolution and accuracy of CMIP6 simulations [17,18]. Traditional methods, such as bilinear interpolation, are simple but often fail to capture high-frequency details, leading to potential inaccuracies in fine-scale predictions [19]. More advanced methods, like CDF-t (probabilistic downscaling) [20] and Support Vector Machines [21], offer improved performance but still have limitations in preserving spatial details and handling complex climate variables [22]. Among these, Convolutional Neural Networks (CNN) have shown promise in generating high-resolution climate data by leveraging deep learning techniques to enhance spatial resolution and model non-linear relationships in climate variables [22,23].

However, CNN models may still have limitations in capturing complex patterns and reducing artifacts, leading to potential inaccuracies in high-resolution climate projections. To overcome these challenges, this study introduces a novel approach using a Generative Adversarial Network (GAN) [24] for downscaling CMIP6 SM data. GAN, compared to a single CNN, offers several advantages, including improved generation of high-resolution data by learning from both real and synthetic samples through adversarial training [25]. This method can better capture complex patterns and reduce artifacts, leading to more accurate and reliable high-resolution SM projections [26]. For instance, GANs have been successfully applied in various remote sensing applications, demonstrating their ability to enhance image quality and detail [27,28].

In this paper, we use the UNet-Gan model to merge and downscale data from 17 CMIP6 models, resulting in the $CMIP6_{UNet\text{-}Gan}$ dataset [29]. This dataset includes SM data for five depth layers (0–10 cm, 10–30 cm, 30–50 cm, 50–80 cm, 80–110 cm), four SSP (SSP1-2.6, SSP2-4.5, SSP3-7.0, SSP5-8.5), and a spatial resolution of 0.1 degrees. The dataset will be used to conduct a trend analysis for the TRSR based on the obtained fine-resolution SM data. In Section 2, we first introduce the study area and provide detailed information about the data used, including ERA5-Land, AMSMQTP data, data from 17 CMIP6 models, and in situ data. We then describe the structure and equations of the UNet-Gan model used in this study, as well as the novel in situ loss function based on in situ soil observations that we introduce for the first time. This section also covers the Mann–Kendall trend analysis method used for trend analysis and the specific implementation details of UNet-Gan. In Section 3, we begin by assessing the accuracy of ERA5-Land and AMSMQTP in the TRSR and validate the accuracy of the $CMIP6_{UNet\text{-}Gan}$ data. We then analyze the spatial distribution of SM change trends and the time series of SM. Finally, we provide the mean values and rates of change of SM for different periods in the TRSR: early 21st century (2021–2040), mid-21st century (2041–2070), and late 21st century (2071–2100).

2. Materials and Methods

2.1. Study Area

The study area is the TRSR, located in the interior of the Tibetan Plateau (TP), China, with coordinates ranging from 89°24′ to 103°30′E and 31° to 37°12′N [6] (seen Figure 1 below). TRSR, also known as the "Chinese Water Tower", contains the headwaters of the Yellow, Yangtze, and Lancang rivers [30]. The TRSR lies at the transition zone between per-

mafrost and seasonally frozen ground, making it a critical area for studying the impacts of permafrost degradation [7]. Covering an area of approximately 363,000 km^2, TRSR includes multiple counties across four Tibetan Autonomous Prefectures in Qinghai Province [31]. The region supports a diverse ecosystem and serves as a vital source of water for millions of people downstream [32]. However, it is also an area where the effects of climate change are most pronounced, leading to shifts in the ecosystem and water availability [8].

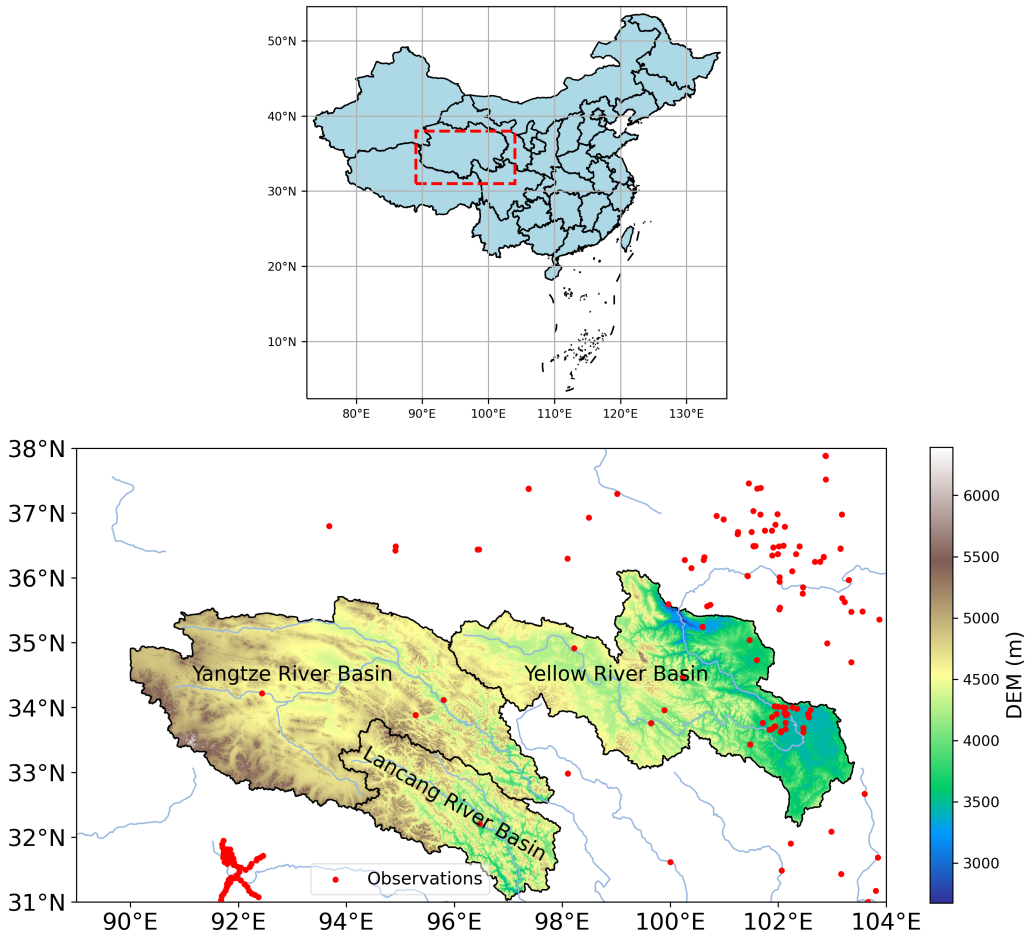

Figure 1. Above is the location of the study area in China, **below** is the elevation of the study area and the location of the in-site.

2.2. Data

2.2.1. ERA5-Land Data

ERA5-Land is a high-resolution reanalysis dataset developed by the European Centre for Medium-Range Weather Forecasts (ECMWF) [33] (https://cds.climate.copernicus.eu/datasets/reanalysis-era5-land-monthly-means?tab=download, accessed on 1 August 2024). It provides a comprehensive and consistent record of land surface variables with a spatial resolution of 9 km and a temporal resolution of one hour, covering the period from 1950 to the present [33]. The use of ERA5-Land data is advantageous in scientific research that requires high-resolution and long-term consistent land surface observations [34]. Its fine spatial and temporal resolutions enable detailed analysis of climate variability, hydrological cycles, and land-atmosphere interactions [35]. Therefore, this study selected monthly SM data from three layers: 0–7 cm, 7–28 cm, and 28–100 cm, as the target variables for the model. The unit of measurement is m^3/m^3, covering the time period from 1950 to 2014. The spatial extent is defined by a rectangular area between 89°E to 104°E and 31°N to 38°N, with 71 grid cells in the latitude and 151 grid cells in the longitude.

2.2.2. AMSMQTP Data

The AMSMQTP dataset is constructed using an automated machine learning algorithm that integrates multi-source meteorological and land surface data, alongside in situ SM observations from the International Soil Moisture Network (ISMN) and the China Meteorological Administration (CMA) [36] (http://www.ncdc.ac.cn/portal/metadata/4d94e0b3-a10c-43f6-b971-23e2df62c8ff, accessed on 1 August 2024). Covering the period from 2000 to 2021, AMSMQTP provides daily SM data for five depth layers ranging from 0 to 110 cm with a spatial resolution of 0.1 degrees. Compared to other datasets, AMSMQTP exhibits the lowest root mean square error (RMSE) and unbiased RMSE (ubRMSE) and the highest correlation coefficient (R) for the TP. The dataset is available in three versions, with AMSMQTP_ensemble being used in this study due to its outstanding robustness and minimal spatial artifacts. For the model fine-tuning phase, we selected SM data from the five layers as target variables. The raw data were averaged monthly and then resampled to match the ERA5-Land grid, covering the time range from 2000 to 2021.

2.2.3. CMIP6 Data

The Coupled Model Intercomparison Project Phase 6 (CMIP6) represents the latest iteration of a collaborative effort to improve climate model projections and enhance our understanding of climate change [12] (https://cds.climate.copernicus.eu/datasets/projections-cmip6?tab=download, accessed on 1 August 2024). CMIP6 includes a comprehensive suite of climate models from various international research institutions, offering a broad range of scenarios to explore future climate conditions [37]. The project aims to provide a robust framework for evaluating model performance, understanding climate variability, and projecting future climate changes. The CMIP6 dataset includes multiple representative concentration pathways (RCPs) and SSP, providing a comprehensive view of possible future climate scenarios [38,39]. This extensive range of scenarios and model outputs facilitates a more nuanced understanding of climate dynamics and helps inform adaptation and mitigation strategies.

This study selects monthly data for the variable "The mass of water in all phases in the upper 10 cm of the soil layer" from 17 CMIP6 model simulations, with the variable unit in kg/m^2. The model details are provided in Table 1. We use the historical data from 1950 to 2014 to train the model on the mapping relationship between CMIP6 data and either ERA5-Land or AMSMQTP multi-layer SM data. Subsequently, data from four SSPs (SSP1-2.6, SSP2-4.5, SSP3-7.0, SSP5-8.5) were selected for model inference. These SSPs were chosen to represent different socio-economic development paths, ranging from sustainable development to high-emission scenarios, and can reflect the impact of different policy and market responses on climate change. Initially, we convert the unit of CMIP6 SM data to m^3/m^3. Due to significant differences in spatial resolution among the 17 CMIP6 models, we perform linear interpolation of the data to match the ERA5-Land grid for ease of subsequent modeling.

Table 1. Details of 17 CMIP6 models.

Model Name	Modelling Centre	Resolution (Lon × Lat)	Used Member
ACCESS-CM2	CSIRO-ARCCSS	1.875° × 1.25°	r1i1p1f1
BCC-CSM2-MR	BCC	1.125° × 1.1215°	r1i1p1f1
CanESM5-CanOE	CCCMA	2.8125° × 2.7906°	r1i1p2f1
CESM2	NCAR	1.25° × 0.9424°	r1i1p1f1
CMCC-CM2-SR5	CMCC	1.25° × 0.9424°	r1i1p1f1
CNRM-CM6-1-HR	CNRM-CERFACS	0.5° × 0.5°	r1i1p1f2
CNRM-ESM2-1	CNRM-CERFACS	1.4° × 1.4°	r1i1p1f2
EC-Earth3-Veg-LR	EC-Earth-Consortium	1.125° × 1.1215°	r1i1p1f1
KACE-1-0-G	NIMS-KMA	1.875° × 1.25°	r1i1p1f1
MIROC6	MIROC	1.4° × 1.4°	r1i1p1f1
MIROC-ES2L	MIROC	2.8125° × 2.7906°	r1i1p1f2

Table 1. *Cont.*

Model Name	Modelling Centre	Resolution (Lon × Lat)	Used Member
MPI-ESM1-2-LR	MPI-M AWI	1.875° × 1.865°	r1i1p1f1
MRI-ESM2-0	MRI	1.125° × 1.1215°	r1i1p1f1
NorESM2-LM	NCC	2.5° × 1.895°	r1i1p1f1
NorESM2-MM	NCC	1.25° × 0.9424°	r1i1p1f1
TaiESM1	AS-RCEC	1.25° × 0.9424°	r1i1p1f1
UKESM1-0-LL	MOHC, NERC, NIMS-KMA, NIWA	1.875° × 1.25°	r1i1p1f2

2.2.4. In Situ Data

The ISMN is a global database that collects, compiles, and provides access to in situ SM measurements from various ground-based observation networks around the world [40,41] (https://ismn.earth/en/, accessed on 1 August 2024). The network comprises over 2600 stations across different climates and land cover types, ensuring a diverse and comprehensive representation of SM conditions. The data provided by ISMN include measurements at various soil depths, these in situ observations are essential for cross-validating satellite-based SM products, enhancing model simulations, and improving our understanding of SM dynamics on a global scale.

In this study, we selected ISMN in situ data within the rectangular area defined by the ERA5-Land dataset, covering the period from May 2008 to September 2019 (with 94 ISMN stations distributed across three observation networks: the CTP_SMTMN [42] network with 56 stations, the MAQU Dente et al. [43] network with 27 stations, and the NAQU [44] network with 11 stations). Additionally, we utilized in situ data from the CMA within the same area from 2015 to 2018 (with 93 CMA stations). The in situ data cover soil depths from 0 to 110 cm, and we averaged the data on a monthly scale. In addition to being used to validate the monthly scale ERA5-Land and AMSMQTP data errors, the in situ data also contribute to the calculation of a portion of the model training loss (in situ loss) for backpropagation.

2.3. Method

In this study, we employ a GAN model, where the historical surface SM data from 17 CMIP6 models are used as the model input (referred to as I^{CMIP6}, with 17 channels), and the five-layer SM data from AMSMQTP (with 5 channels) are used as the model's target output. By learning the mapping relationship between CMIP6 and AMSMQTP during the historical period, the trained model is then applied to infer CMIP6 data under four emission scenarios (SSP1-2.6, SSP2-4.5, SSP3-7.0, SSP5-8.5). This results in five-layer SM data (0–10 cm, 10–30 cm, 30–50 cm, 50–80 cm, 80–110 cm) for the TRSR from 2015 to 2100, with a temporal resolution of one month and a spatial resolution of 0.1 degrees, referred to as $\mathrm{CMIP6}_{\mathrm{UNet\text{-}Gan}}$.

To enhance the model's performance and robustness, our training process is divided into two stages. The first stage is the pretraining phase, where ERA5-Land data are used as the target output. The second stage is the fine-tuning phase, with AMSMQTP data as the target output. During the fine-tuning phase, the initialization values of the model parameters, except for the last convolutional layer, are derived from the parameters obtained in the pre-training phase, while the initial values of the last convolutional layer are randomly initialized. It is noteworthy that during the fine-tuning phase, we also calculate the in situ loss, as illustrated in Figure 2. Finally, we employ the Mann–Kendall trend analysis [45] to examine the trends in $\mathrm{CMIP6}_{\mathrm{UNet\text{-}Gan}}$ under the four emission scenarios.

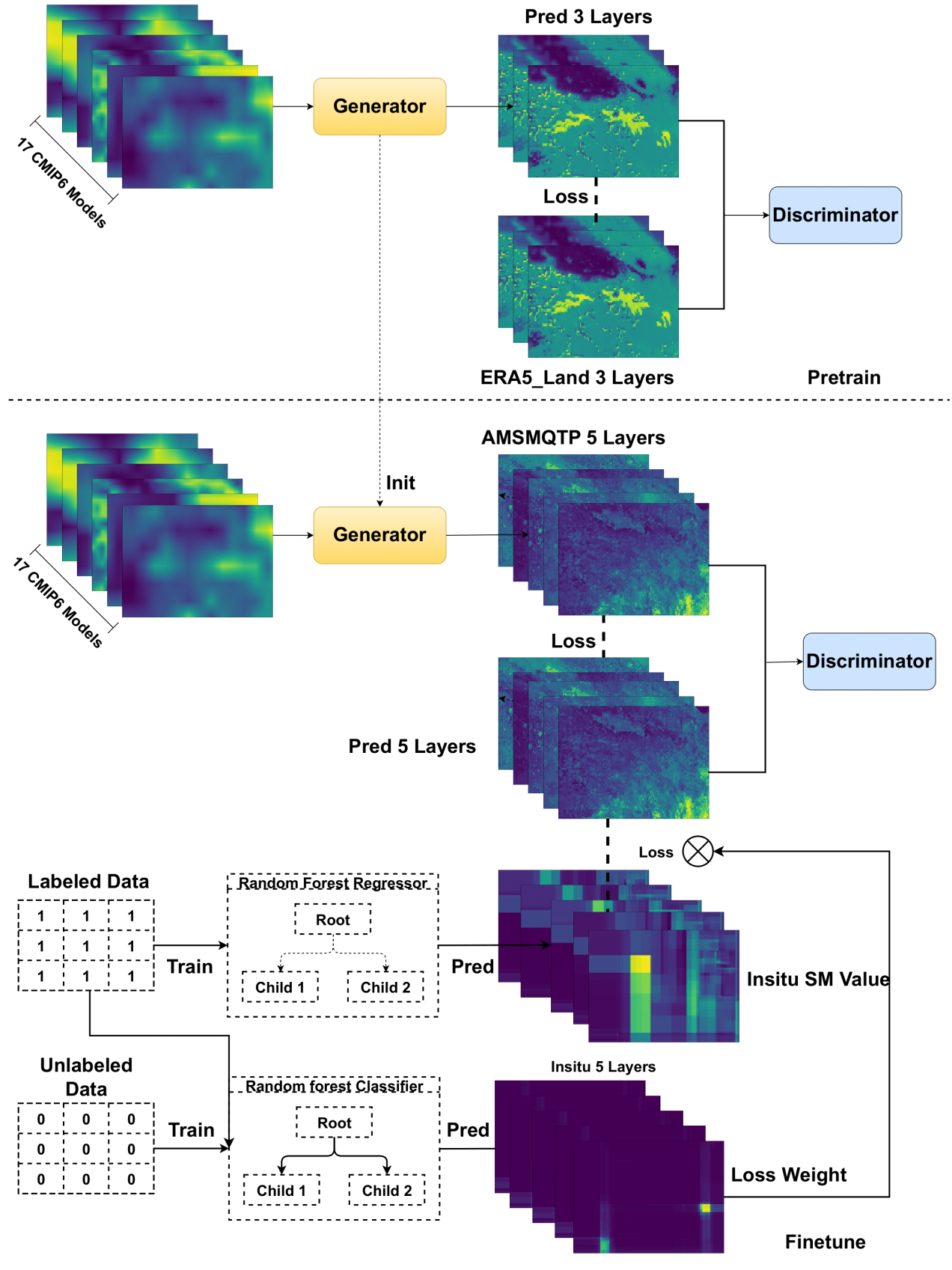

Figure 2. Training details of the UNet-GAN network.

2.3.1. UNet-Gan

GAN is a class of deep learning models consisting of two neural networks: a generator and a discriminator, which are trained simultaneously through an adversarial process. The generator aims to produce data that mimic the real data distribution, while the discriminator's role is to distinguish between real data and the data generated by the generator. During training, the generator learns to create increasingly realistic data by trying to fool the discriminator, and the discriminator improves its ability to differentiate between real and synthetic data. This adversarial setup leads to the generator producing high-quality, realistic outputs.

In the context of this study, we utilize a GAN architecture where the generator is based on a UNet structure, which is well-suited for tasks requiring detailed pixel-level predictions, such as SM mapping [46]. The generator takes input from CMIP6 historical SM data and attempts to generate corresponding high-resolution SM data, while the discriminator evaluates the generated outputs against the target data. The goal is to train the generator to produce SM outputs that are indistinguishable from the real data, ensuring that the model captures the complex relationships between the input and output datasets. This method allows for the generation of accurate future projections of SM under various climate scenarios. Our optimization objective is an adversarial min-max problem, where (D_{θ_D}) is the discriminator, (G_{θ_G}) is the generator, (I_{CMIP6}) represents the CMIP6 data, and (I_{Target}) represents ERA5-Land during the pretraining phase and AMSMQTP during the fine-tuning phase. The formula is as follows:

$$\min_{\theta_G}\max_{\theta_D}\mathbb{E}_{I^{Target}\sim p_{\text{train}}(I^{Target})}[\log D_{\theta_D}(I^{Target})]+ \mathbb{E}_{I^{CMIP6}\sim p_G(I^{CMIP6})}[\log(1-D_{\theta_D}(G_{\theta_G}(I^{CMIP6})))] \tag{1}$$

- **Generator**

  The U-Net architecture is a convolutional neural network (CNN) designed for image segmentation tasks, particularly in biomedical imaging [47]. It has a symmetric architecture comprising two main parts: a contracting path (encoder) and an expansive path (decoder). The contracting path captures context by downsampling the input image through successive convolutional and pooling layers, effectively extracting high-level features. The expansive path then upsamples these features, reconstructing the spatial resolution while combining them with corresponding high-resolution features from the contracting path via skip connections. These skip connections help preserve spatial information that might otherwise be lost during the downsampling process, allowing for precise localization of features.

  In this study, we employ a U-Net architecture as the generator within a GAN framework; the model structure is shown in Figure 3. The U-Net's ability to accurately capture and reconstruct spatial features makes it particularly suitable for generating high-resolution SM data from lower-resolution inputs. By leveraging the U-Net structure, the model can effectively learn the mapping between coarse CMIP6 inputs and the corresponding high-resolution AMSMQTP or ERA5-Land outputs, ensuring that fine-scale details are preserved in the generated SM predictions. The optimization objective for the generator is expressed by the following equation:

$$\hat{\theta}_G = \arg\min_{\theta_G}\frac{1}{N}\sum_{n=1}^{N} l^G(G_{\theta_G}(I_n^{CMIP6}), I_n^{Target}, I_n^{In-situ}) \tag{2}$$

  The l^G loss function is a weighted average of several losses, including content loss, total variation Loss [48], adversarial loss [49], and a novel auxiliary loss method specifically designed for the Earth sciences, referred to as in situ loss. The calculation methods for each type of loss will be described in detail in the following sections.

- **Discriminator**
  The model structure of the discriminator is shown in Figure 4. It first processes the input through a convolutional layer and a leaky ReLU activation, followed by seven convolutional blocks. The output is then mapped to a one-dimensional value through a dense layer and a sigmoid layer, representing the probability that an image is real or fake, with values ranging from 0 to 1. The optimization objective for the discriminator is as follows:

$$\begin{aligned}\hat{\theta}_D = \arg\min_{\theta_D} & -log(D_{\theta_D}(I^{Target}) - \mathbb{E}[D_{\theta_D}(G_{\theta_G}(I^{CMIP6}))]) \\ & -log(1-(D_{\theta_D}(G_{\theta_G}(I^{CMIP6}))) - \mathbb{E}[D_{\theta_D}(I^{Target})])\end{aligned} \tag{3}$$

  The above formula calculates the relative loss between I^{CMIP6} and the I^{Target}, where the expectation operation $\mathbb{E}$ is computed over each minibatch [49].

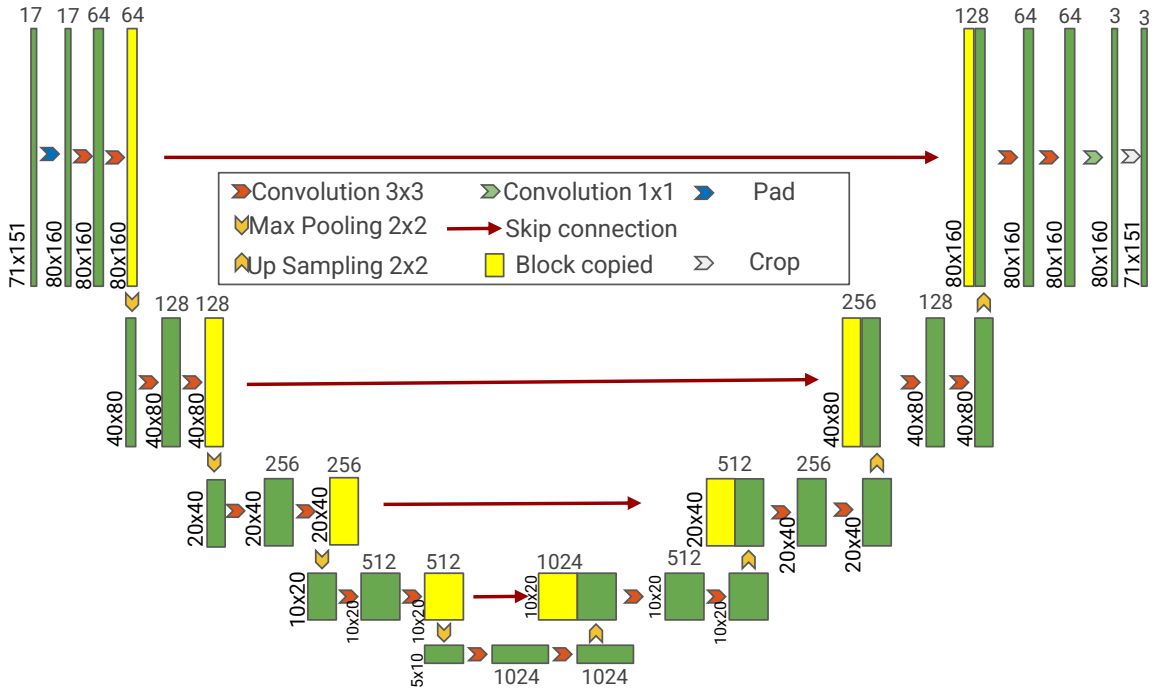

Figure 3. The model structure of U-Net (with three output channels for the pretraining phase and five output channels for the fine-tuning phase).

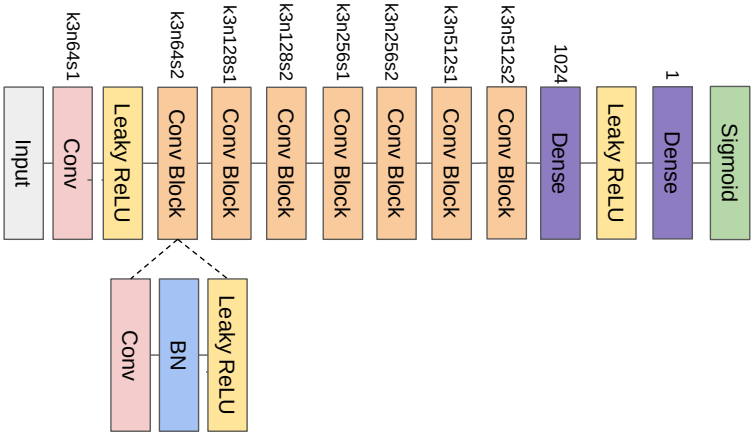

Figure 4. The model structure of the discriminator. The number following *k* indicates the convolution kernel size, the number following *n* indicates the number of output channels, and the number following *s* indicates the stride.

2.3.2. Generator's Loss Function

The loss function for the generator is given by the following formula (all losses are computed only within the vector boundaries of the TRSR):

$$l^G = \alpha_1 l^G_{Content} + \alpha_2 l^G_{Adv} + \alpha_3 l^G_{In-situ} + \alpha_4 l^G_{TV} \tag{4}$$

- **Content loss**

Mean squared error (MSE) loss measures the average of the squared differences between predicted and target values, providing a direct assessment of prediction accuracy. It is commonly used in regression tasks within generator models, as it penalizes larger errors more heavily, encouraging the model to produce outputs closer to the true values. In the following formula, H represents the number of latitude pixels, W represents the number of longitude pixels, and C represents the number of soil layers.

$$l^G_{MSE} = \frac{1}{CWH} \sum_{x=1}^{W} \sum_{y=1}^{H} \sum_{z=1}^{C} (I^{Target}_{x,y,z} - G_{\theta_G}(I^{CMIP6})_{x,y,z})^2 \tag{5}$$

VGG Loss, based on the VGG network, captures perceptual differences by comparing high-level features between generated and target images, helping to produce visually more realistic results [48]. It is particularly effective in preserving texture and fine details, as it measures the similarity in feature space rather than directly comparing pixel values [48]. In this study, the pre-trained VGG16 model is used, where i and j represent the starting and ending layers of the pre-trained model, respectively. $\phi_{i,j}$ denotes a portion of the pre-trained model, and $H_{i,j}$, $W_{i,j}$, and $C_{i,j}$ represent the height, width, and number of channels of the feature map produced by $\phi_{i,j}$. In this paper, i and j are set to 0 and 30 (both inclusive), respectively. The formula is as follows:

$$\begin{aligned} l^G_{VGG/i.j} = \frac{1}{W_{i,j} H_{i,j} C_{i,j}} \sum_{x=1}^{W_{i,j}} \sum_{y=1}^{H_{i,j}} \sum_{z=1}^{C_{i,j}} (\phi_{i,j}(I^{Target})_{x,y,z} \\ - \phi_{i,j}(G_{\theta_G}(I^{CMIP6}))_{x,y,z})^2 \end{aligned} \tag{6}$$

The content loss is obtained by a weighted combination of the two loss functions mentioned above, as expressed in the following formula:

$$l^G_{Content} = \beta_1 l^G_{MSE} + \beta_2 l^G_{VGG/i,j} \tag{7}$$

- **Adversarial loss**

The formula for the adversarial loss is similar to that of the discriminator loss, but the optimization objective is completely opposite. We aim for $G_{\theta_G}(I^{CMIP6})$ to be closer to real data than I^{Target}. The formula is as follows:

$$l^G_{Adv} = -log(D_{\theta_D}(G_{\theta_G}(I^{CMIP6})) - \mathbb{E}[D_{\theta_D}(I^{Target})]) \tag{8}$$

- **In-situ loss**

In situ observations are generally considered the most accurate means of measuring SM, which is why this paper introduces a novel in situ loss as an auxiliary loss. The main process is illustrated in Figure 2. Our key idea is to convert point-based in situ observations into spatial grids. We first use Random Forest [50] Regression, training it with five simple features (soil layer, latitude, longitude, year, and month) to infer $I^{In-situ}$. Additionally, we employ a Random Forest Classifier using the same five features, where labeled data are assigned a class of 1, the pseudocode is shown in Algorithm 1. We then randomly sample unlabeled data from the spatial domain (matching the number of labeled data points for class balance) and assign them a class of 0. The classifier is trained and used to infer I^{Prob}, which indicates the reliability of the data, with values ranging from 0 to 1. The formula for calculating in situ loss is as follows:

$$l_{In-situ}^{G} = \frac{1}{CWH} \sum_{x=1}^{W} \sum_{y=1}^{H} \sum_{z=1}^{C} [I_{x,y,z}^{Prob} (I_{x,y,z}^{In-situ} - G_{\theta_G}(I^{CMIP6})_{x,y,z})^2] \quad (9)$$

Algorithm 1 Random Forest Classifier for In Situ Observations

Input: Labeled dataset $D_l = \{(x_i, 1)_{i=1...n}\}$, where x_i are the features. Unlabeled dataset $D_u = \{(x_j, 0)\}$

Output: Inferred class probabilities I^{Prob} for unlabeled data

1: Randomly sample n unlabeled data points
2: Assign class 0 to sampled points
3: $RF \leftarrow$ RandomForestClassifier($n\_estimators = k$)
4: RF.fit($D_{combined}$)
5: $I^{Prob} \leftarrow RF$.predict_proba(D_u)
6: **return** I^{Prob}

- **Total Variation Loss**
  Total Variation (TV) Loss is incorporated into the generator's loss function to promote spatial smoothness in the generated outputs while preserving essential image structures. By minimizing the differences between neighboring pixels, TV Loss reduces noise and prevents the introduction of artifacts, ensuring that the generated SM maps maintain coherent and natural-looking spatial patterns. This loss is particularly effective in enhancing the visual quality of generated images, making them more realistic and consistent with physical processes.

$$l_{TV}^{G} = \sum_{x=1}^{W} (I_{x,y} - I_{x-1,y})^2 + \sum_{y=1}^{H} (I_{x,y} - I_{x,y-1})^2 \quad (10)$$

2.3.3. Mann–Kendall Trend Analysis

The Mann–Kendall test is a non-parametric statistical method used to identify trends in time series data, particularly for environmental and climate data [6]. It assesses whether a monotonic trend exists in a dataset without assuming any specific distribution for the data. The test is widely used due to its robustness and minimal assumptions, making it suitable for various types of time series data, including those with missing values or outliers.

The Mann–Kendall test evaluates the null hypothesis H_0 that there is no trend in the data against the alternative hypothesis H_1 that a trend exists. The test statistic S is calculated as follows:

$$S = \sum_{i=1}^{n-1} \sum_{j=i+1}^{n} \text{sgn}(X_j - X_i) \quad (11)$$

where $sgn(x)$ is the sign function, which returns 1 if $x > 0$, -1 if $x < 0$, and 0 if $x = 0$. X_i and X_j are the data values at time i and j, respectively. n is the number of observations.

The variance of S under the null hypothesis is given by the following:

$$\text{Var}(S) = \frac{n(n-1)(2n+5) - \sum_{t=1}^{k} (n_t(n_t-1)(2n_t+5))}{18} \quad (12)$$

where k is the number of tied groups, and n_t is the number of observations in the t-th tied group.

To determine the significance of the trend, the standardized test statistic Z is computed:

$$Z = \begin{cases} \frac{S-1}{\sqrt{\text{Var}(S)}} & \text{if } S > 0 \\ 0 & \text{if } S = 0 \\ \frac{S+1}{\sqrt{\text{Var}(S)}} & \text{if } S < 0 \end{cases} \quad (13)$$

The value of Z is compared against critical values from the standard normal distribution to assess statistical significance. Typically, a significance level of 0.05 is used, with a positive Z indicating an upward trend and a negative Z indicating a downward trend.

The significance of the trend is evaluated based on the magnitude of Z. If the absolute value of Z exceeds the critical value from the normal distribution (e.g., ± 1.96 for a 95% confidence level), the null hypothesis H_0 is rejected, indicating a statistically significant trend in the data. If $|Z|$ is less than the critical value, the trend is not considered statistically significant.

To quantify the magnitude of the trend, Sen's slope estimator Q is used. It is computed as:

$$Q = \text{median}\left(\frac{X_j - X_i}{j - i}\right) \tag{14}$$

where the median is taken over all pairs (i, j) with $i < j$. This estimator provides a robust measure of the trend's rate.

In this study, the Mann–Kendall test is applied to assess the significance of trends in the generated SM data under various emission scenarios. This analysis helps identify significant changes in SM over time, contributing to a better understanding of the impacts of climate change on SM dynamics.

2.3.4. Evaluation Metrics

MAE measures the average magnitude of errors between predicted and observed values, providing an intuitive indication of the model's overall prediction accuracy.

$$\text{MAE}(y, \hat{y}) = \frac{1}{n_{\text{samples}}} \sum_{i=0}^{n_{\text{samples}}-1} |y_i - \hat{y}_i|. \tag{15}$$

RMSE quantifies the square root of the average squared differences between predicted and observed values, emphasizing larger errors and giving a sense of how well the model captures extreme deviations.

$$\text{RMSE}(y, \hat{y}) = \frac{1}{n_{\text{samples}}} \sum_{i=0}^{n_{\text{samples}}-1} \sqrt{(y_i - \hat{y}_i)^2}. \tag{16}$$

MAPE expresses the error as a percentage of the observed values, allowing for a normalized measure of prediction accuracy, particularly useful when comparing errors across different scales.

$$\text{MAPE}(y, \hat{y}) = \frac{1}{n_{\text{samples}}} \sum_{i=0}^{n_{\text{samples}}-1} \frac{|y_i - \hat{y}_i|}{\max(\epsilon, |y_i|)} \tag{17}$$

In the above equations, ϵ is a small but strictly positive number introduced to avoid undefined results when y is zero.

Pearson R assesses the linear correlation between predicted and observed values, indicating how well the model captures the strength and direction of the relationship between the two datasets.

$$\text{R}(y, \hat{y}) = \frac{\sum_{i=0}^{n_{\text{samples}}-1} (y_i - \overline{y_i})(\hat{y}_i - \overline{\hat{y}_i})}{\sqrt{\sum_{i=0}^{n_{\text{samples}}-1} (y_i - \overline{y_i})^2} \sqrt{\sum_{i=0}^{n_{\text{samples}}-1} (\hat{y}_i - \overline{\hat{y}_i})^2}} \tag{18}$$

2.3.5. Implementation Details

In the pretrain stage, data from 1950 to 1999 were used as the training set, data from 2000–2007 were used as the validation set, and data from 2008 to 2014 were used as the test set. In the fine-tuning stage, the data spanned from 2000 to 2014, and we employed five-fold

cross-validation. Our model was implemented using the PyTorch 2.2 [51] framework, and all experiments were conducted on an NVIDIA Tesla V100-SXM2 32 GB GPU. We manually searched for hyperparameter settings and ultimately chose a batch size of 100, 200 epochs, a learning rate of 5×10^{-4} for the generator, and 1×10^{-6} for the discriminator. The size of all convolution kernels in the UNet was set to 3. We applied early stopping, with the patience set to 10 epochs, and also used a cosine learning rate decay strategy. The loss weights were set as follows:

$$\beta_1 = 1, \beta_2 = 0.006, \alpha_1 = 1, \alpha_2 = 0.001, \alpha_3 = 0.01, \alpha_4 = 4 \times 10^{-8} \quad (19)$$

3. Results and Analysis

3.1. Accuracy Comparison of ERA5-Land and AMSMQTP Data in the TRSR

As shown in Figure 5, by comparing the errors and accuracy between the in situ SM and the corresponding grid SM from AMSMQTP and ERA5-Land, AMSMQTP exhibits higher accuracy across all layers compared to ERA5-Land (which is also why we use AMSMQTP in the fine-tuning stage). Additionally, based on the R metric, we observe that for both datasets, the median R decreases as depth increases. As shown in Table S1, the median R for Layer 1 of AMSMQTP is 0.918, and for Layer 5, it is 0.658; the median R for Layer 1 of ERA5-Land is 0.659, and for Layer 5, it is 0.250. We also find that although AMSMQTP's data accuracy is significantly better than that of ERA5-Land, the distribution of its evaluation metrics exhibits a long-tail distribution (i.e., there are some outliers), indicating that AMSMQTP still has lower accuracy at certain points. This is one of the reasons we introduce in situ loss in this paper.

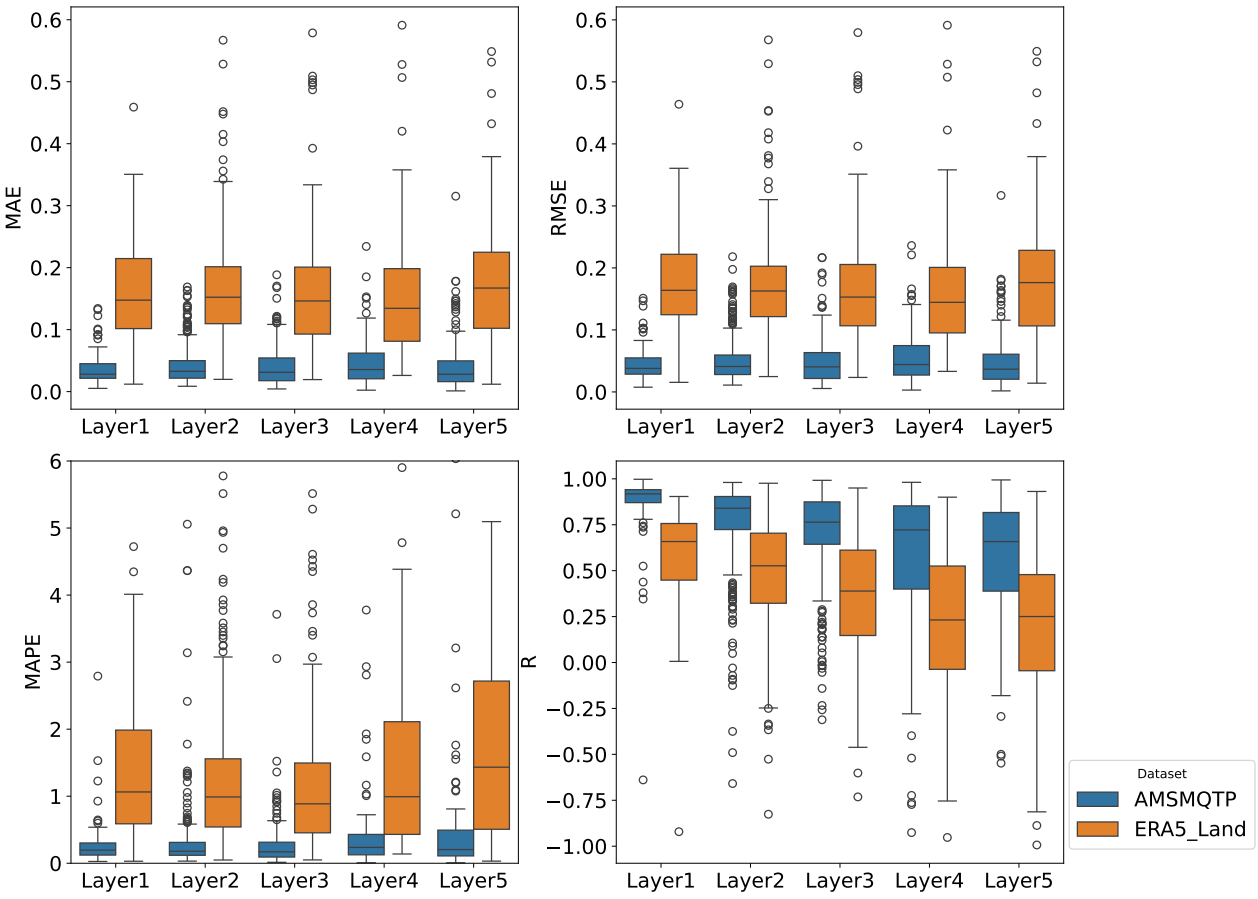

Figure 5. Box plots of evaluation metrics for SM from different layers of ERA5-Land and AMSMQTP compared to in situ observations (for MAE, RMSE, and MAPE, smaller values are better, and for R, larger values are better).

3.2. Evaluation of CMIP6$_{UNet\text{-}Gan}$

Figure 6 demonstrates the performance of UNet-Gan in data fusion and downscaling for the 17 CMIP6 datasets (with the actual values being the AMSMQTP data). We observe that UNet-Gan effectively integrates and downscales CMIP6 data for the five SM layers. However, data accuracy shows a decreasing trend with increasing depth, except for the fourth layer. The R^2 values are 0.819, 0.802, 0.694, 0.778, and 0.541, respectively, and the R values are 0.905, 0.895, 0.833, 0.882, and 0.736, respectively. Figure 7 shows a comparison of the data predicted by the UNet-Gan model for the first layer in the test set with the data from 17 CMIP6 models and their Ensemble, against the AMSMQTP data. We found that UNet-Gan achieved the highest correlation coefficient, and its standard deviation is very close to that of AMSMQTP, indicating similar variability. Additionally, UNet-Gan also achieved the lowest RMSE. We also observed that five CMIP6 models had correlation coefficients less than 0, and the Ensemble did not achieve the highest correlation coefficient, except for UNet-Gan. This may be due to some CMIP6 models having poor accuracy in the TSRS.

As shown in Figures 6 and 7, UNet-Gan achieved the best performance. We applied the bagging method to the five models obtained from five-fold cross-validation and performed data fusion and downscaling for the 17 CMIP6 datasets across historical periods and four emission scenarios. This resulted in the TSRS five-layer SM data for historical periods (1950–2014) and the four future emission scenarios (2015–2100), with a spatial resolution of 0.1 degrees and a temporal resolution of one month. We refer to this dataset as CMIP6$_{\text{UNet-Gan}}$.

3.3. Spatial Distribution of SM Trends Under Four Emission Scenarios

As shown in Figure 8, SM in Layer 1 exhibits a significant increasing trend within the TRSR under all four emission scenarios. The areas with the highest rates of moisture increase are concentrated in the western part of the Yangtze River and the southeastern part of the Yellow River. Layer 2 shows a trend similar to that of Layer 1. In Layer 3, in addition to the two regions with high moisture increase rates seen in Layer 1, the northeastern part of the Yellow River also emerges as a high-value area. For Layer 4, regions with high moisture increase rates are only found in small areas of the northeastern and southeastern parts of the Yellow River. In Layer 5, under the SSP1-2.6 scenario, the high moisture increase rate is concentrated in much of the Yangtze River area, while the other three emission scenarios do not show significant concentrated high-value areas. Across all five layers, there is a consistent pattern where moisture increase rates rise with higher SSP scenarios, and the rate of increase slows with increasing depth. Figures corresponding to Layer 2 through Layer 5, which depict similar content to Figure 8, are provided in the Supplementary Materials.

As shown in Figure 9, Layer 1 exhibits a significant increasing trend in SM during winter across the entire TRSR under all four emission scenarios, with the highest moisture increase located in the southeastern part of the Yellow River. In spring, the entire TRSR also shows a significant moisture increase, with the highest rates mainly concentrated in much of the Yangtze River region and a small part of the southern Yellow River area. During summer, the regions with significant moisture increases are much smaller; under the SSP1-2.6 scenario, only a small portion of the northern Yangtze River passes the significance test. As the SSP increases, the area passing the significance test gradually expands, but the highest moisture increase is still confined to the northwestern part of the Yangtze River. In autumn, the entire TRSR exhibits a significant increasing trend, with the highest moisture increase concentrated in most of the Yangtze River region.

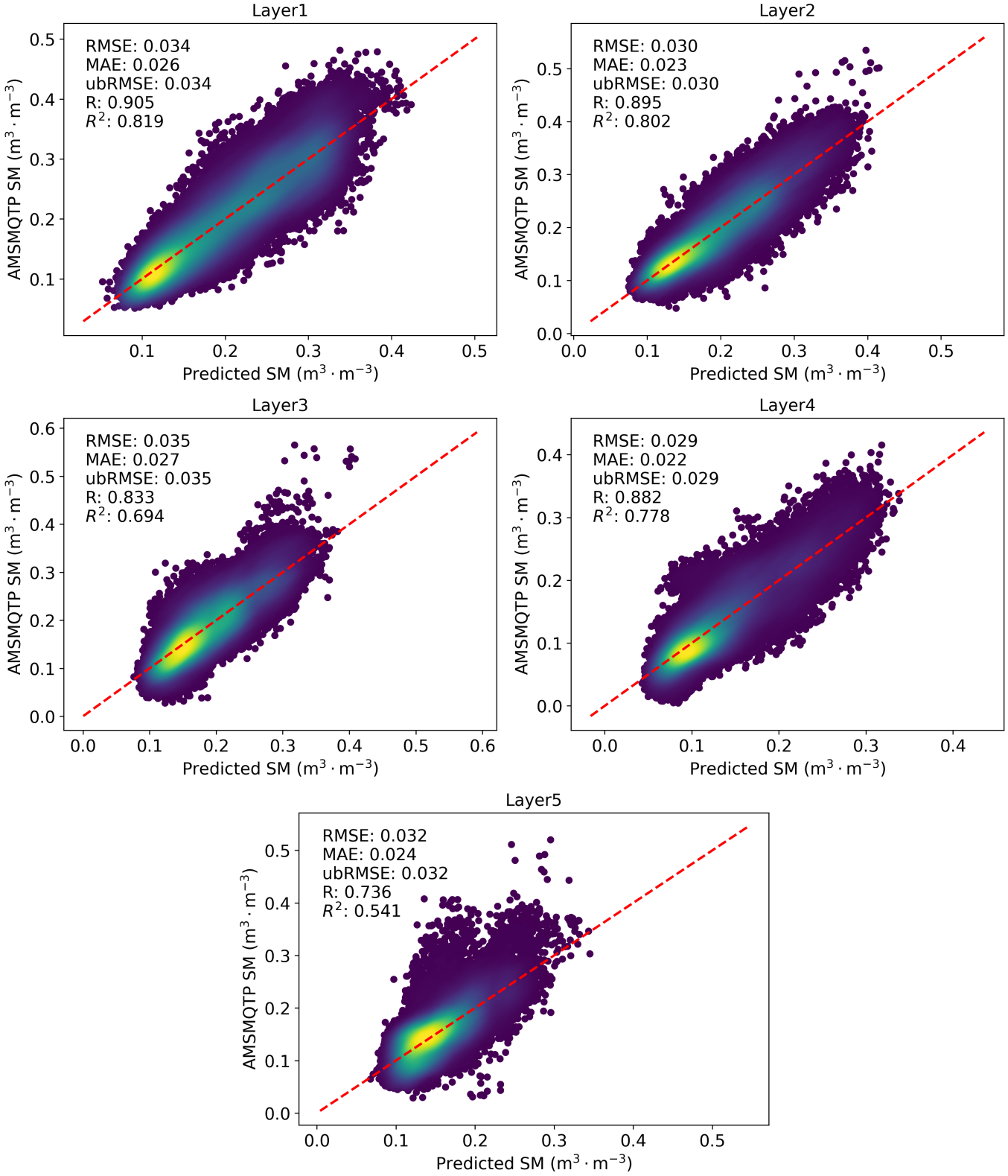

Figure 6. Scatter plot of predicted values versus true values on the test set for five-fold cross-validation (The red dotted line represents a 45-degree diagonal, and the color intensity indicates the density of the points).

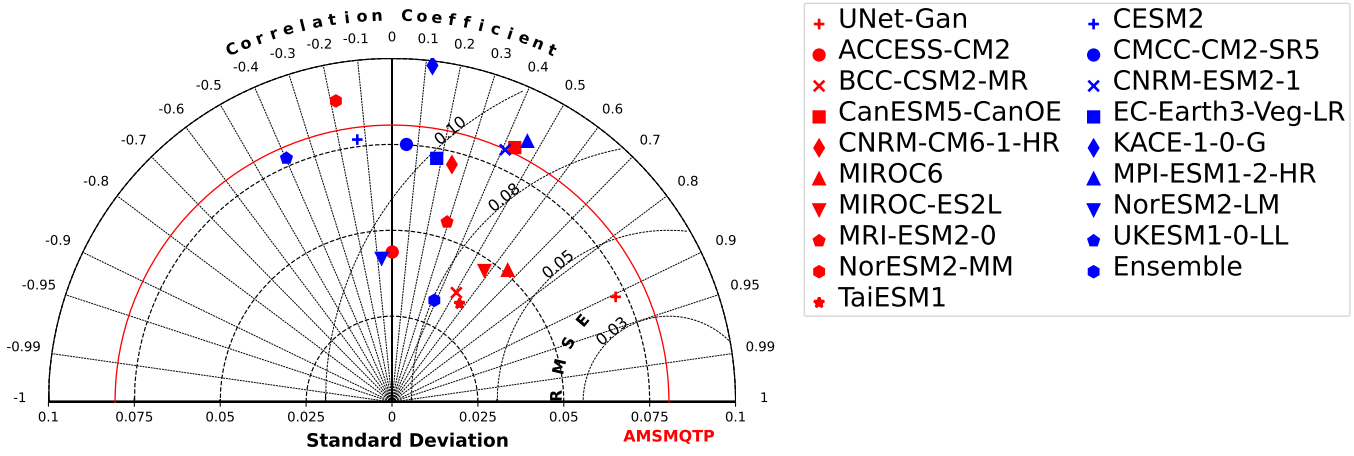

Figure 7. A comparison of the data predicted by the UNet-Gan model for the first layer in the test set with the data from 17 CMIP6 models and their Ensemble, against the AMSMQTP data. The diagram includes three metrics: RMSE, standard deviation, and correlation coefficient.

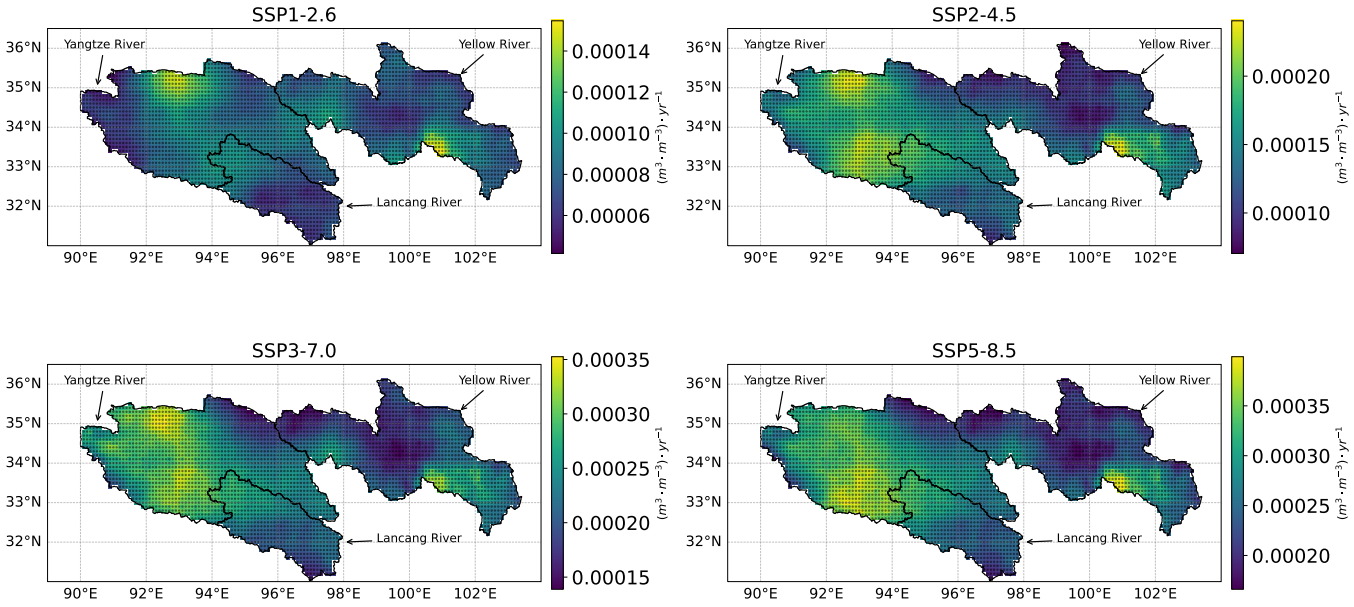

Figure 8. Spatial distribution of the annual mean SM trends for Layer 1 under four emission scenarios, with dotted areas indicating regions significant at the 95% confidence level.

From Figure 9, we observe that across all four seasons, SM increase rates rise with higher SSP scenarios. The summer season shows the smallest area and rate of significant moisture increase, while the other three seasons display a significant moisture increase across the entire TRSR, with winter showing the highest increase rate. Layers 2 and 3 show similar seasonal trends to Layer 1, while Layers 4 and 5 have smaller areas that pass the significance test, and the moisture increase rate in deeper layers slows compared to the upper layers across all seasons. Figures corresponding to Layers 2 through 5, which depict similar content to Figure 9, are provided in the Supplementary Materials. We focus only on regions that pass the significance test, disregarding those that do not, and find that nearly all areas that pass the significance test exhibit a trend of increasing moisture.

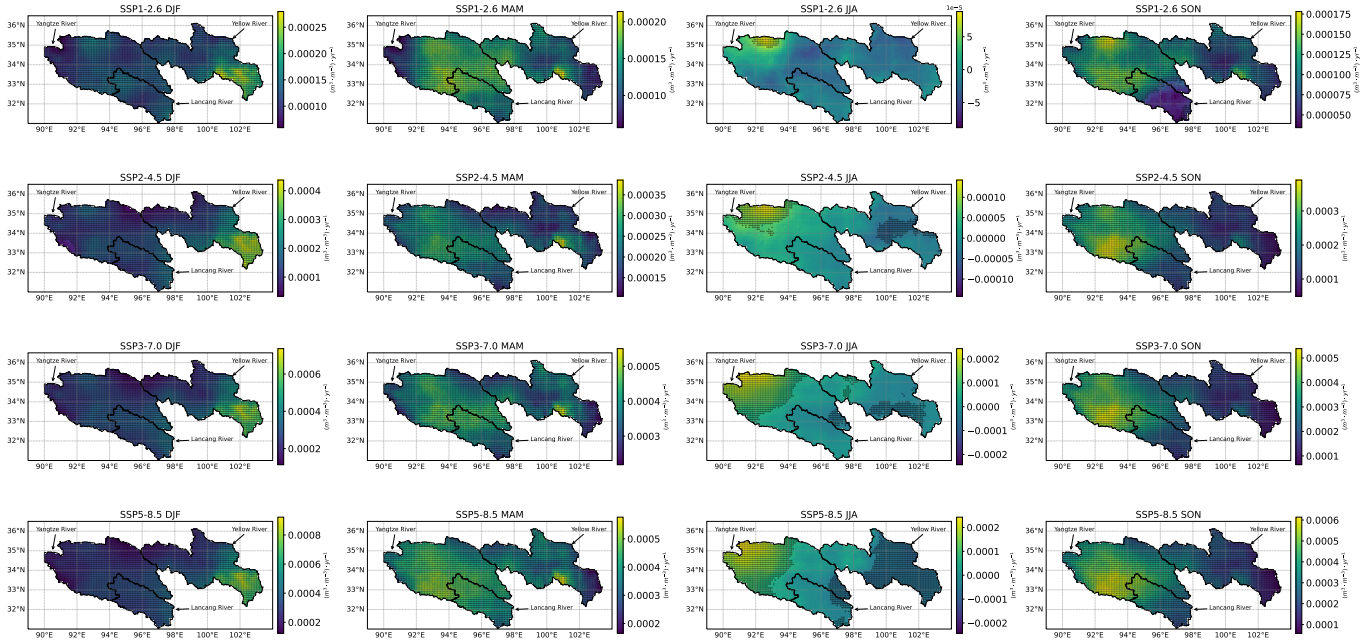

Figure 9. Spatial distribution of annual average SM trend changes in Layer 1 under four emission scenarios for different seasons, with highlighted areas indicating significance at the 95% confidence level (DJF represents winter, MAM represents spring, JJA represents summer, and SON represents autumn).

3.4. Time Series of SM in the TRSR

As shown in Figure 10, the annual average SM for Layer 1 in the TRSR region and three sub-regions exhibits a significant increasing trend under both historical and four emission scenarios. The moisture increase rates for the Historical scenario are similar to those for SSP1-2.6. Specifically, the increase rate for Historical is slightly lower than SSP1-2.6 in the TRSR and Yangtze River regions, while it is slightly higher in the Yellow River and Lancang River regions. Additionally, the increase rate grows with higher SSP scenarios, with Layer 1 showing increase rates of 8.49×10^{-5}, 1.54×10^{-4}, 2.43×10^{-4}, and 2.73×10^{-4} $(m^3 \cdot m^{-3}) \cdot yr^{-1}$, respectively. Similar results are observed for the other layers. Figures for Layers 2 through 5, which are similar to Figure 10, are provided in the Supplementary Materials. We also find that as depth increases, the moisture increase rates in the TRSR and three sub-regions show a decreasing trend under both the Historical and the four emission scenarios.

As shown in Figures 11 and 12, under the four future emission scenarios, Layer 1 SM exhibits a significant increasing trend in winter, spring, and autumn, with the highest increase rate observed in spring. As SSP increases, the moisture increase rates in the TRSR region are as follows: 1.53×10^{-4}, 2.33×10^{-4}, 3.89×10^{-4}, and 4.02×10^{-4} $(m^3 \cdot m^{-3}) \cdot yr^{-1}$ for spring; 1.39×10^{-4}, 1.58×10^{-4}, 3.01×10^{-4}, and 3.41×10^{-4} $(m^3 \cdot m^{-3}) \cdot yr^{-1}$ for winter; and 1.02×10^{-4}, 2.07×10^{-4}, 2.86×10^{-4}, and 3.36×10^{-4} $(m^3 \cdot m^{-3}) \cdot yr^{-1}$ for autumn. In summer, no significant increase trend is observed in the TRSR region. As shown in the time series in Figure 12a, the summer series under the four emission scenarios remains stable, fluctuating around a certain mean. Layer 2 shows a similar time series to Layer 1. However, from Layer 3 onward, significant moisture increase rates are observed in summer under SSP3-7.0 and SSP5-8.5 scenarios. The increase rates are as follows: 3.96×10^{-5} and 2.52×10^{-5} $(m^3 \cdot m^{-3}) \cdot yr^{-1}$ for Layer 3; 4.01×10^{-5} and 2.15×10^{-5} $(m^3 \cdot m^{-3}) \cdot yr^{-1}$ for Layer 4; and 4.42×10^{-5} and 2.74×10^{-5} $(m^3 \cdot m^{-3}) \cdot yr^{-1}$ for Layer 5. For these three layers, the rate under SSP5-8.5 is lower than that under SSP3-7.0. For winter, autumn, and summer, the time series for Layers 3 to 5 is similar to that of Layer 1, with a decreasing trend in moisture increase rate as depth increases. Figures for Layers 2 through 5, similar to Figures 11 and 12, are provided in the Supplementary Materials.

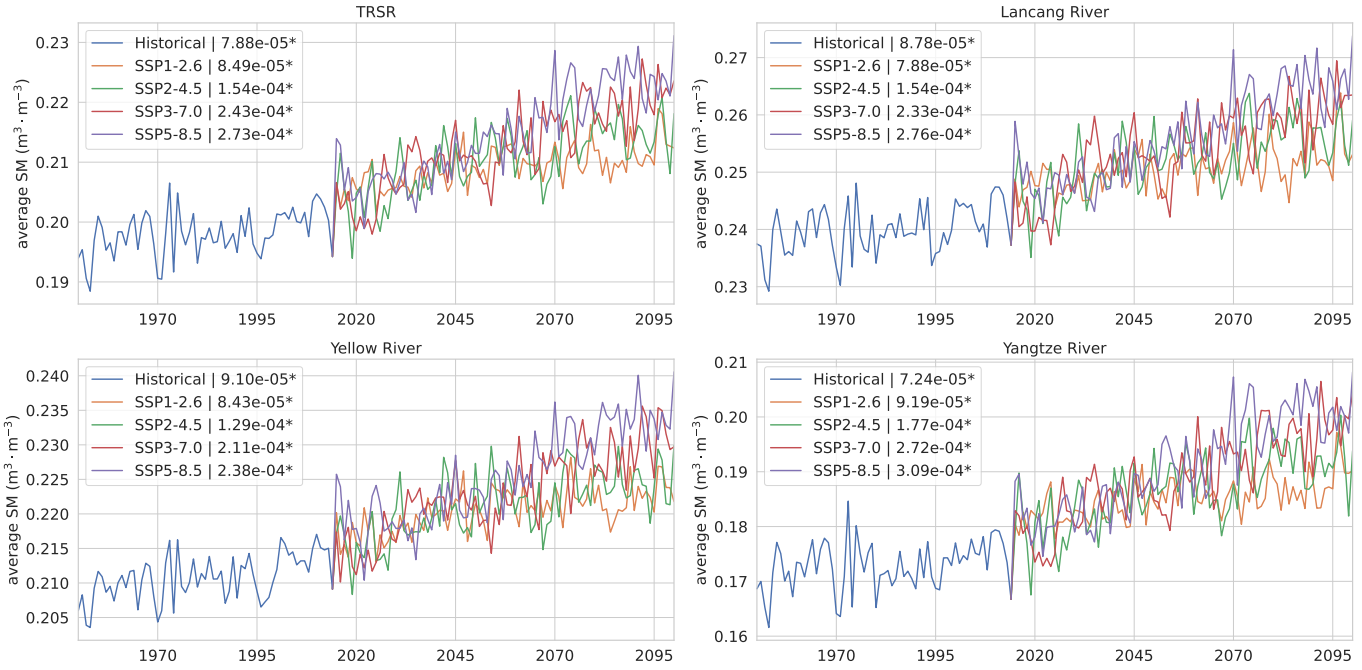

Figure 10. Time series of annual average SM for Layer 1 under different historical and future emission scenarios. The legend provides the rate of change, with units in m^3/m^3 per year, and asterisks indicate significance at the 95% confidence level.

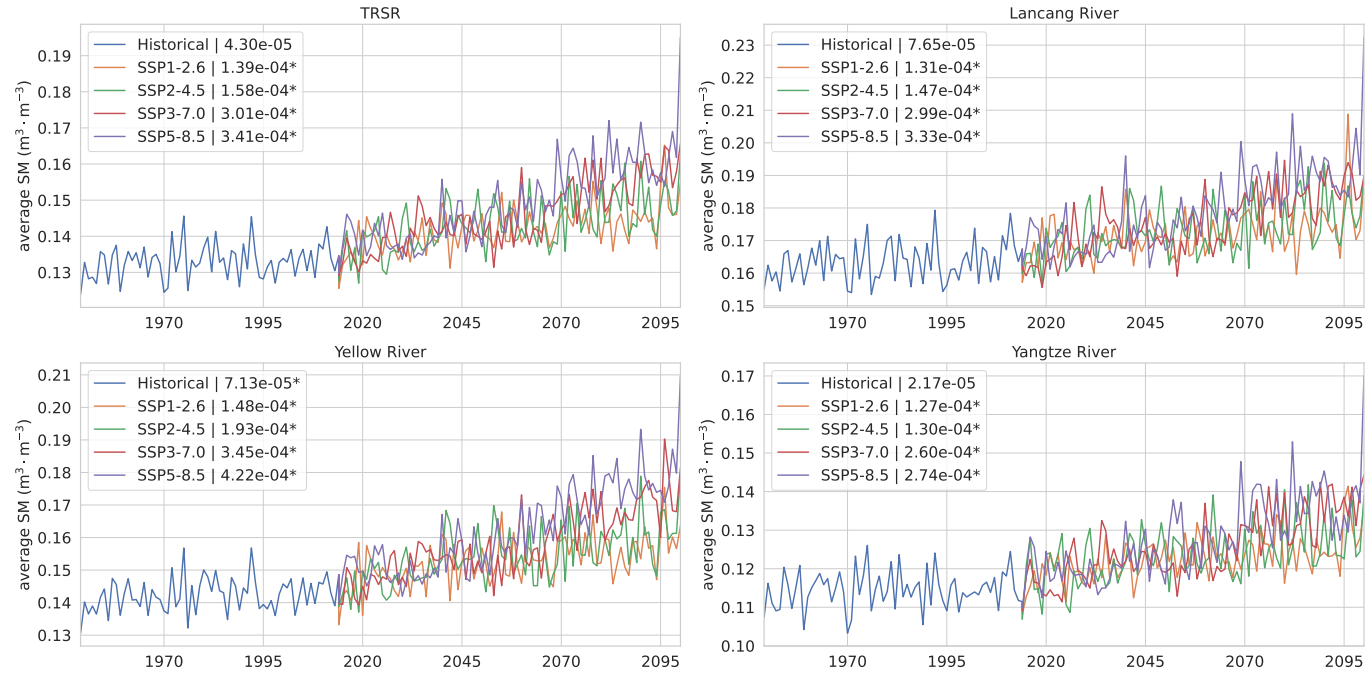

(**a**) DJF

Figure 11. *Cont.*

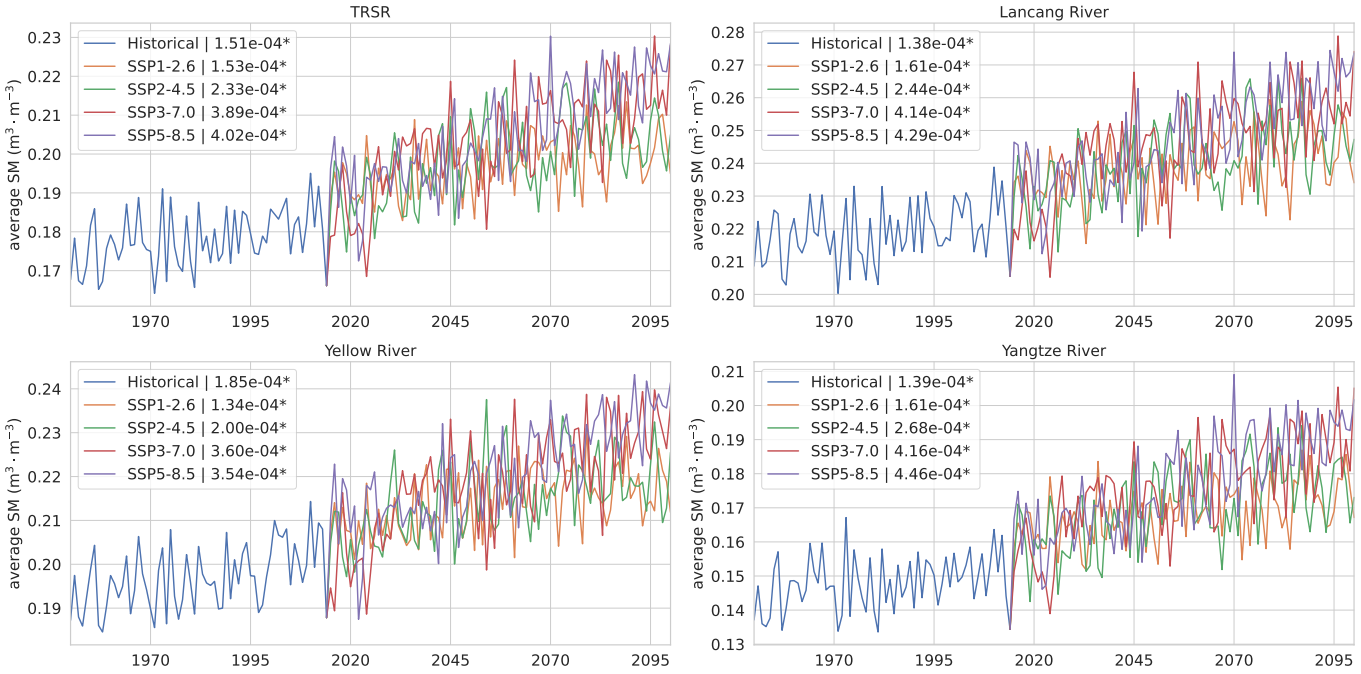

(**b**) MAM

Figure 11. Time series of annual average SM for Layer 1 under historical and future emission scenarios in different seasons, with the legend showing the rate of change in units of m^3/m^3 per year. Asterisks indicate significance at the 95% confidence level (DJF represents winter, MAM represents spring, JJA represents summer, and SON represents autumn).

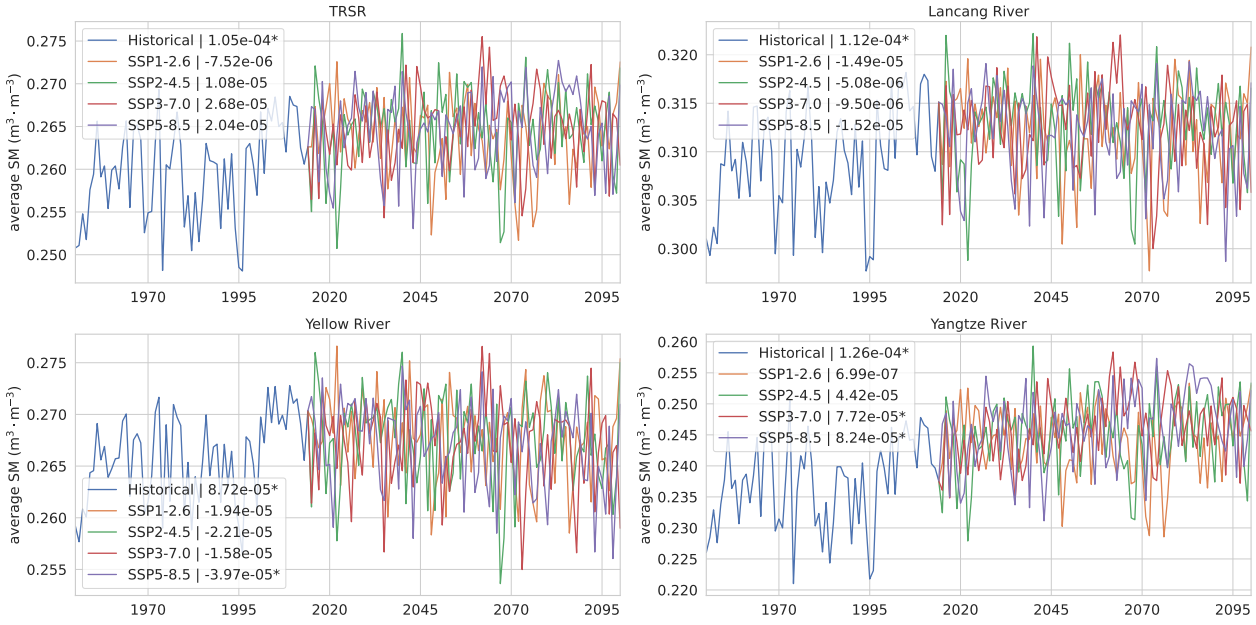

(**a**) JJA

Figure 12. *Cont.*

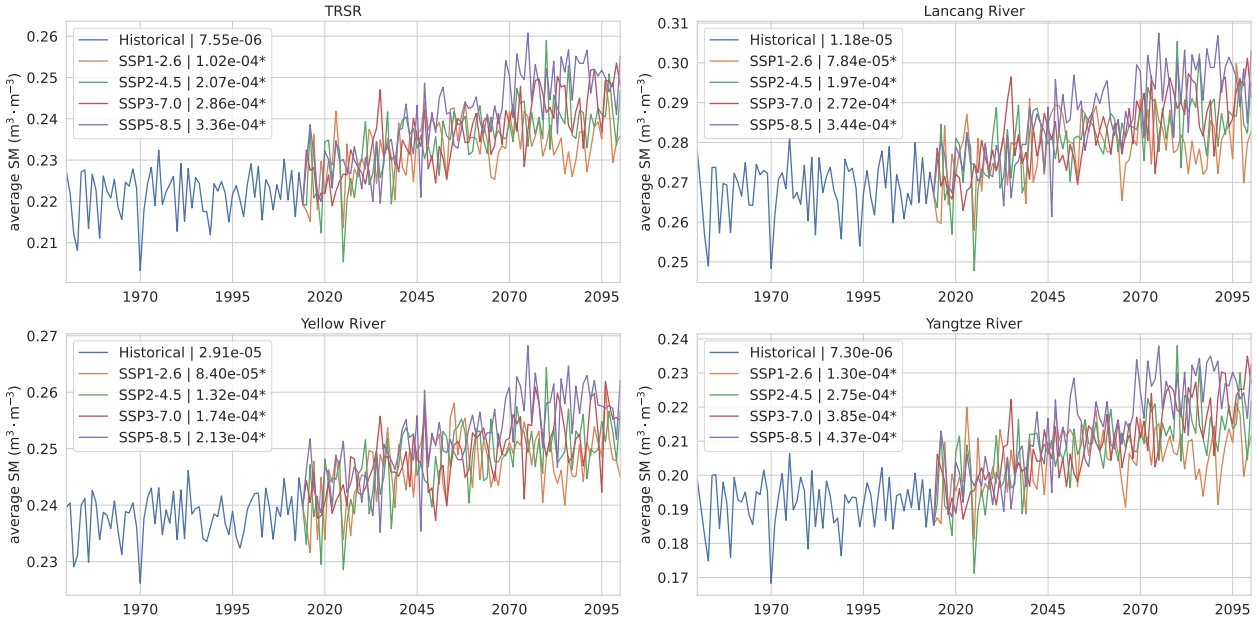

(**b**) SON

Figure 12. Same as Figure 11, but for JJA and SON.

3.5. Temporal TRSR SM and Its Rate of Change

For the Historical period, we selected the years 1995–2014, and for the four future scenarios, we chose the periods 2021–2040, 2041–2070, and 2071–2100. The reasons for studying these three sub-periods are as follows: First, the impacts of climate change may vary across different time periods. By dividing the 21st century into three sub-periods, we can more clearly analyze the effects of climate change on SM, observe how these effects evolve over time, and identify potential turning points. Second, different time periods may correspond to the implementation of different policies and adaptation measures. For instance, measures taken in the early 21st century may differ from those in the mid and late periods. Analyzing SM change trends across different time periods helps assess the effectiveness of policies and adjust future response strategies.

As shown in Figure 13, the average annual SM shows a clear upward trend by the end of this century. For the surface layer (Layer 1), the increase between 1995 and 2014 and 2071–2100 ranges from 5.5% to 11.5%, with significant rises in spring (10.5–19.9%) and winter (9.8–20.3%), while autumn (5.4–12.1%) and summer (0.8–1.1%) exhibit more modest increases. A similar pattern is seen in Layer 2, where the overall increase varies from 4.6% to 9.2%. Spring and winter again show the most notable changes (8.2–14.8% for MAM and 8.1–16.2% for DJF), while summer remains relatively stable (0.8–1.3%) and autumn experiences a moderate increase (3.7–8.4%).

The trend continues in deeper layers. In Layer 3, SM rises by 4.3–7.5%, with the largest increases observed in spring (6.1–11.2%) and winter (6.3–12.0%). Autumn and summer increases are smaller, particularly in summer (0.9–1.9% for JJA). In Layer 4, the rise ranges from 4.5% to 7.5%, with spring and winter increases again leading (7.1–12.7% for MAM and 7.1–14.3% for DJF), and summer contributing the least (1.3–2.0% for JJA). Finally, in Layer 5, the increase is between 3.3% and 6.5%, with the greatest growth observed in spring (5.4–9.5%) and winter (5.8–10.8%), while autumn and summer experience relatively smaller increases (1.9–4.4% for SON and 1.8–2.4% for JJA).

For all layers, spring and winter exhibit the strongest increases in SM, with autumn showing moderate changes and summer exhibiting the smallest gains. Furthermore, as the depth of the soil increases, the growth rate of SM tends to diminish. By the end of the century, the mean SM under the SSP5-8.5 scenario is projected to be the highest across all layers, whereas SSP1-2.6 results in the lowest values.

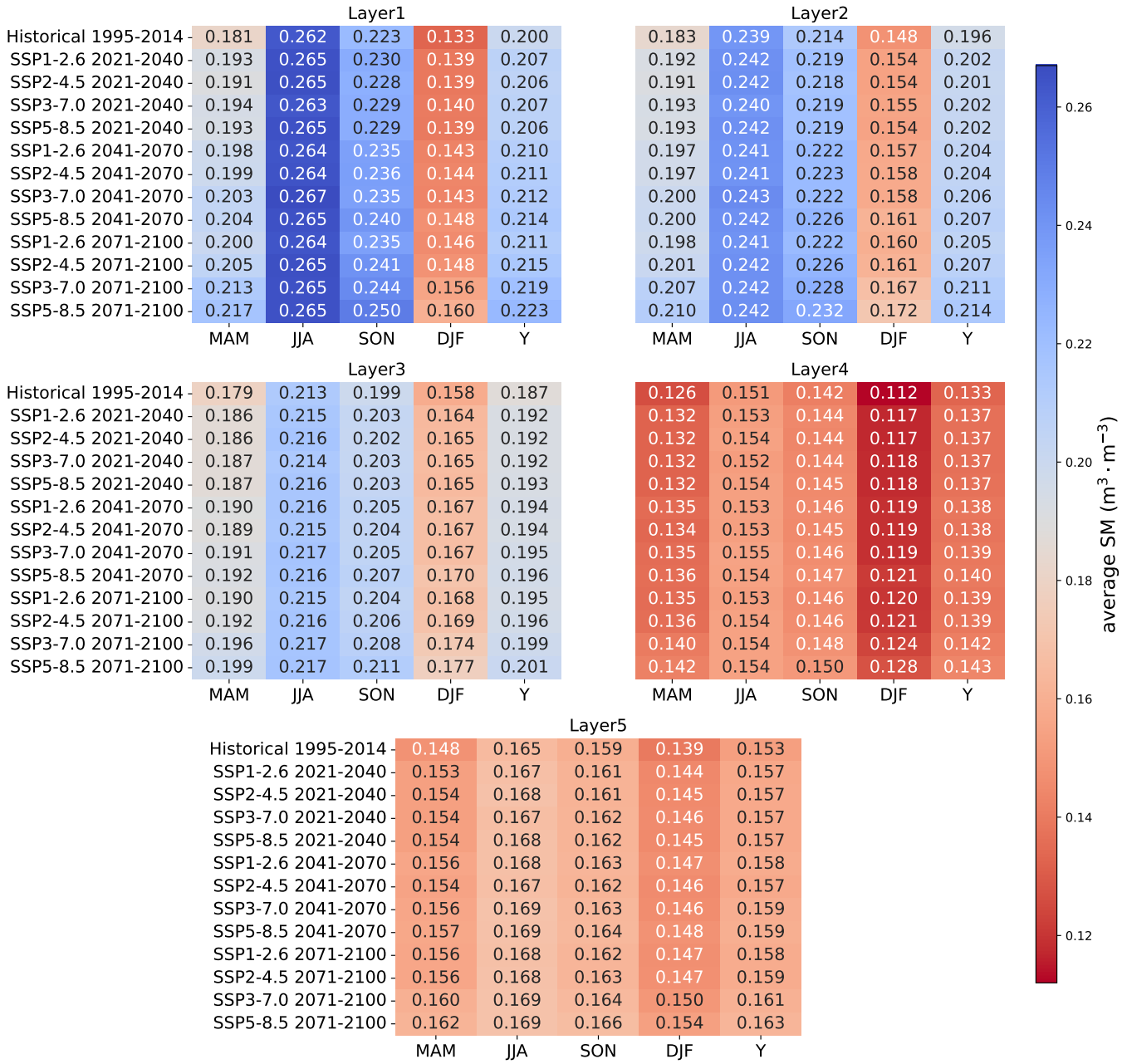

Figure 13. The mean SM of the five layers in TRSR over different periods, with the Historical period covering 1995–2014, and the four emission scenarios covering 2021–2040, 2041–2070, and 2071–2100, respectively. MAM, JJA, SON, and DJF represent mean SM values for spring, summer, autumn, and winter, respectively, while Y represents the mean annual SM.

Figure 14 shows the percentage increase in SM for Layer 1 under four emission scenarios at the end of the 21st century (2071–2100) compared to the beginning of the century (1995–2014). The northwest corner of the Yangtze River shows a significant moisture increase, ranging from approximately 12% to 20% under higher SSP scenarios. This can be attributed to several factors. Regional climate change is driving shifts in atmospheric circulation, leading to more moisture being transported to the area and an increase in precipitation frequency and intensity. Warmer temperatures also raise the atmosphere is water vapor holding capacity, promoting more rainfall and higher SM. Precipitation patterns in the region may change, with more rainfall during the growing season, particularly influenced by the East Asian summer monsoon. Additionally, the region's topography, including mountains, may enhance moisture accumulation through the orographic effect,

trapping moisture in the area. The spatial distribution maps for Layers 2–5 (provided in the Supplementary Materials) show that moisture increases extend to deeper soil layers but diminish with depth. By Layers 4 and 5, moisture increases become more uniform across regions, with a small moisture increase observed in the southeast corner of the Yellow River, particularly in Layers 4 (2% to 4%) and 5 (1% to 2%).

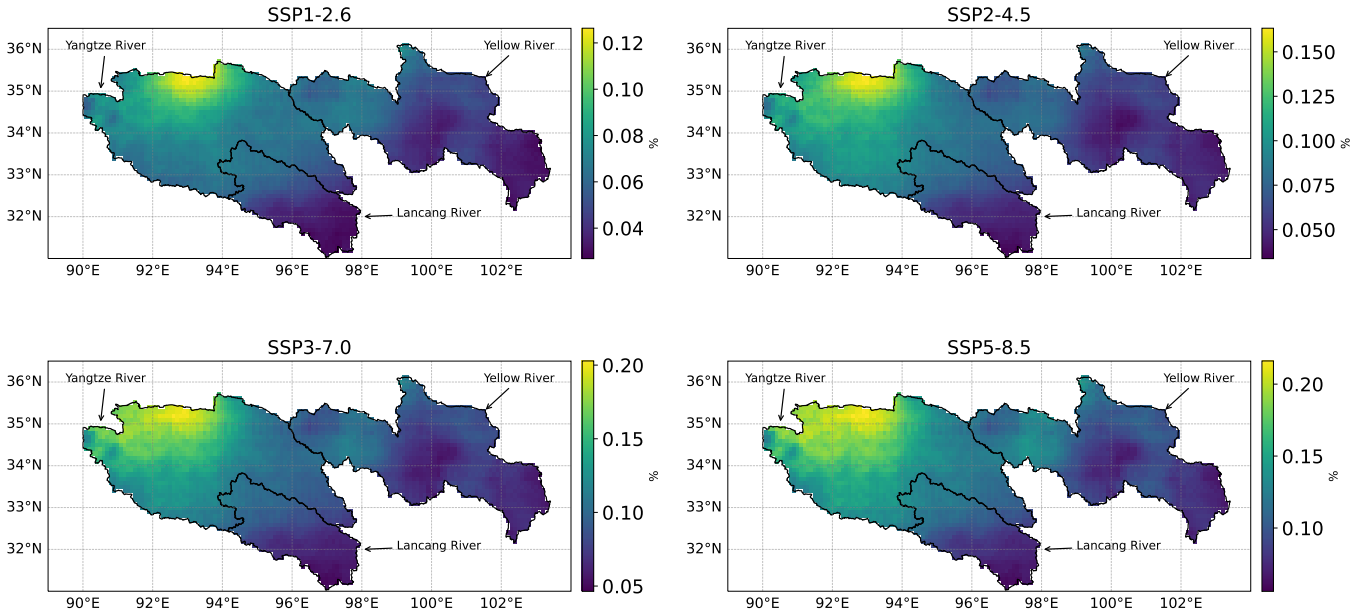

Figure 14. The spatial distribution of the percentage increase in Layer 1 SM under four emission scenarios for the end of the 21st century (2071–2100) compared to the beginning of the century (1995–2014).

Figure 15 shows the SM change rates that passed the 95% significance test. From 1995 to 2014, only the top three layers exhibited a wetting trend, which decreased with depth (annual average rates are 3.303×10^{-4}, 2.437×10^{-4}, and 1.205×10^{-4} $(m^3 \cdot m^{-3}) \cdot yr^{-1}$, respectively). Layers 4 and 5 did not pass the significance test. In the future four emission scenarios, the spring wetting rate for the five layers in the SSP3-7.0 scenario from 2021 to 2040 was the highest, at 1.522×10^{-3}, 1.052×10^{-3}, 6.513×10^{-4}, 4.832×10^{-4}, and 3.377×10^{-4} $(m^3 \cdot m^{-3}) \cdot yr^{-1}$, respectively, and decreased with depth. From Figure 15, it can be inferred that for all five soil layers, the wetting rate is generally highest in spring. Regarding the annual SM change rate, for all five layers, significant wetting mainly occurs in the early 21st century (2021–2040) and the late 21st century (2071–2100), with almost no significant trends in the mid-21st century (2041–2070). Additionally, the wetting rate in the early 21st century is generally higher than in the late 21st century. Seasonally, significant wetting trends are mainly concentrated in spring and winter, while significant wetting trends are less common in summer and autumn, and significant wetting trends decrease with depth.

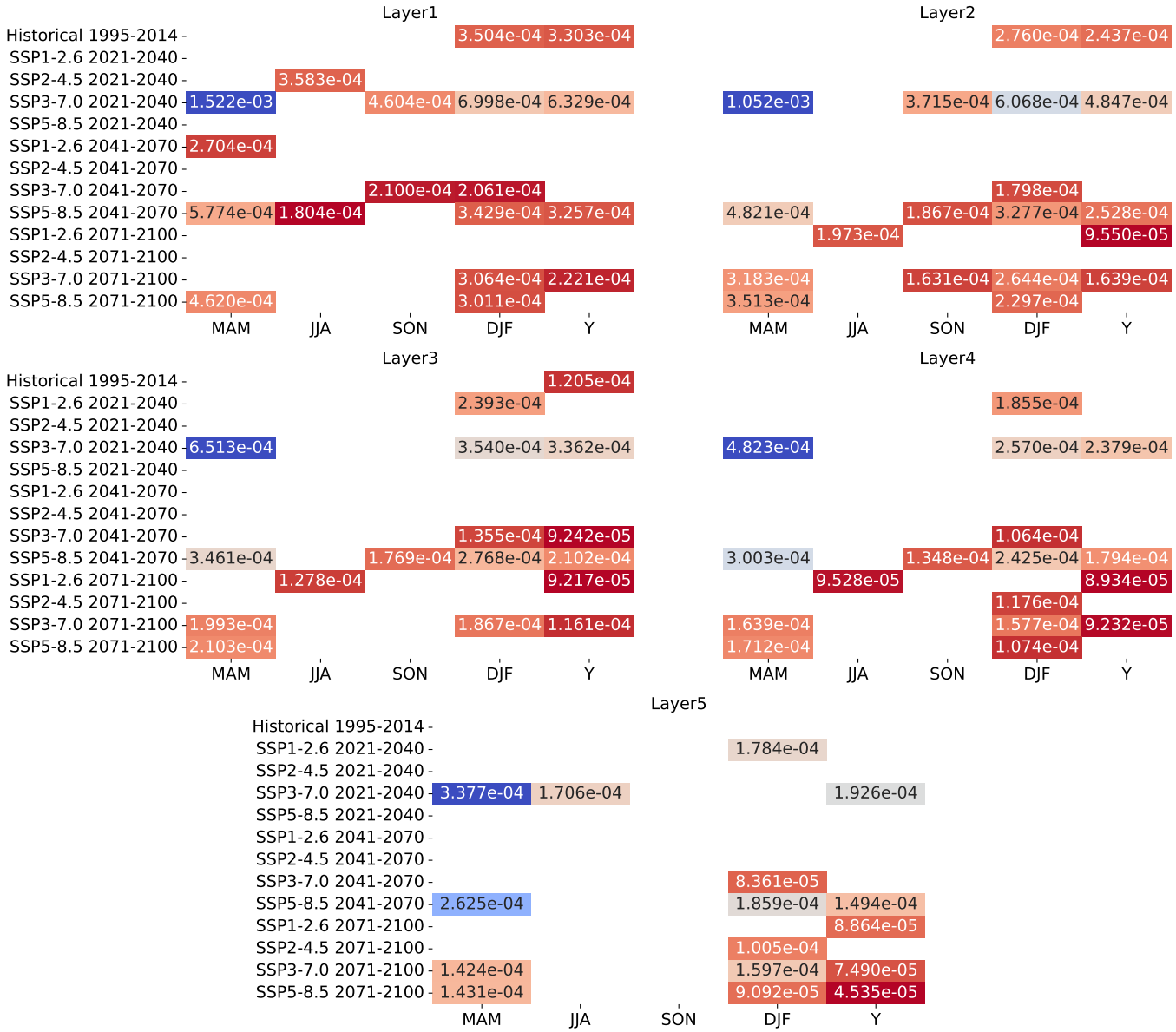

Figure 15. The rate of change in SM for the five layers in TRSR over different periods, with the Historical period covering 1995–2014, and the four emission scenarios covering 2021–2040, 2041–2070, and 2071–2100, respectively. Rates that did not pass the 95% significance test are not shown in the figure. MAM, JJA, SON, and DJF represent the rate of SM change for spring, summer, autumn, and winter, respectively, while Y represents the annual rate of SM change, with units in m^3/m^3 per year.

4. Discussion

This study investigated the spatial and temporal trends of SM change in the TRSR region under four emission scenarios (SSP1-2.6, SSP2-4.5, SSP3-7.0, SSP5-8.5) using UNet-Gan downscaled climate data. The results revealed several key findings, which we now discuss in light of existing knowledge and potential future directions.

The observed slower response of deeper soil layers to climate change, compared to shallower layers, can be attributed to several factors. One key reason is the dampening effect of the upper layers. Changes in surface temperature and precipitation primarily impact the near-surface SM. This moisture then percolates downward through the soil profile, but the process is often slow and subject to several constraints. The infiltration rate is influenced by factors such as soil texture, structure, and porosity. For example, finer soils,

like clay, retain water more tightly, which can slow the downward movement of moisture. Coarser soils, such as sandy ones, may allow quicker infiltration but can lose moisture more rapidly at depth due to lower retention capacity [52].

Moreover, rainfall infiltration is also heavily influenced by external factors such as terrain, precipitation intensity, and duration. In hilly or mountainous regions, runoff can be significant, leading to less moisture infiltration into the soil, especially on slopes where gravity accelerates water movement over the surface. The intensity and duration of rainfall also play crucial roles: heavy, short-duration rains can cause surface runoff before the moisture has a chance to penetrate deeply, whereas light, steady rainfall may allow more effective infiltration, although it may not always reach deeper layers if the soil surface becomes too dry [53]. The interaction of these factors complicates the percolation process and contributes to the slower response of deeper soil layers to changes in surface conditions.

Additionally, the higher thermal inertia of deeper soils further dampens their response to climate change. Deeper soils experience slower temperature fluctuations compared to shallower layers, which results in a delayed response to changes in surface conditions. This slower thermal response leads to a dampened effect on moisture exchange processes, as heat transfer is more gradual at greater depths [54].

In terms of seasonal variations, SM increases significantly in spring and winter, followed by autumn, with the least increase observed in summer. This can be explained by several factors. In spring and winter, lower evaporation rates combined with increased precipitation—especially snowmelt in winter, as future projections indicate earlier melting and delayed freezing [55] in the TRSR region—help retain more moisture in the soil. In contrast, during summer, rising future temperatures lead to higher evapotranspiration [56], reducing the availability of significant SM increases, even if precipitation levels might be higher during the rainy season. This interaction between precipitation and temperature drives the observed seasonal variations.

This study presents a comprehensive analysis of SM trends under four SSP emission scenarios, but several limitations remain. First, the study does not provide detailed insights into the potential biases introduced by land surface conditions, such as surface lithology or geomorphology, although this may not be as important in deep learning, and these factors may play a crucial role in shaping SM dynamics. Moreover, the interaction between local precipitation and temperature, which directly influences SM, lacks in-depth discussion. Although this study obtained SM data for the future TRSR region at a 0.1-degree spatial resolution, which is a significant improvement over the spatial resolution of individual CMIP6 models, future research should focus on addressing these limitations by using higher-resolution satellite products and more reliable validation methods to improve the spatial accuracy of SM estimates [57,58]. Additionally, future studies should explore the influence of surface characteristics (such as vegetation cover, lithology, and geomorphic types) on SM distribution to gain a more detailed understanding of the observed spatial trends. Moreover, future work could delve into the impacts of SM changes under different SSP scenarios on the regional water cycle, vegetation dynamics, and carbon cycle, providing a more comprehensive perspective on the broader environmental effects of SM trends.

5. Conclusions

First, by comparing the SM data accuracy between ERA5-Land and AMSMQTP in the TRSR, we found that AMSMQTP data exhibit superior accuracy across all depth layers compared to ERA5-Land. However, despite AMSMQTP's overall better performance, its evaluation metrics still show a long-tail distribution, indicating lower accuracy at certain locations. This suggests that, although AMSMQTP offers notable advantages, additional correction measures, such as the in situ loss method proposed in this study, are necessary to further improve data accuracy in practical applications.

Second, based on the evaluation of the UNet-Gan model, we observed its outstanding performance in data fusion and downscaling. UNet-Gan successfully integrated and downscaled 17 CMIP6 datasets, demonstrating high-accuracy predictive performance across

five SM layers. Particularly in Layer 1, UNet-Gan achieved the highest correlation coefficient and showed a standard deviation very close to the actual data, further demonstrating its potential in SM data processing. However, as the depth increases, the data accuracy tends to decline, which requires further attention and optimization in future research.

Third, by utilizing the UNet-Gan model to generate more refined and accurate future data at a 0.1-degree spatial resolution for four emission scenarios (SSP1-2.6, SSP2-4.5, SSP3-7.0, SSP5-8.5) ($CMIP6_{UNet\text{-}Gan}$), the following observations were made:

- Overall Increasing Trend in SM: SM in the TRSR and its sub-regions shows a significant increasing trend across all five layers, with higher emission scenarios (SSP5-8.5) leading to faster increases.
- Spatial Distribution Characteristics: There is spatial heterogeneity in SM increase rates among different soil layers in various regions of the TRSR. For instance, the high-value areas for moisture increase rates in Layer 1 and Layer 2 are mainly concentrated in the western part of the Yangtze River and the southeastern part of the Yellow River. In deeper layers (Layer 3 to Layer 5), the distribution of high-value areas changes, particularly with high-value areas emerging in the northeastern part of the Yellow River.
- Decrease in SM Increase Rate with Depth: The rate of moisture increase decreases with increasing depth from Layer 1 to Layer 5. This phenomenon is significant throughout the year and across all seasons, indicating that deeper soils respond more slowly to climate change compared to shallower soils.
- Seasonal Variations in Moisture Increase Trends: Among the four seasons, spring and winter exhibit the most significant moisture increase trends, with the highest increase rates, while summer and autumn show fewer significant moisture increase trends. Particularly in summer, the significant moisture increase areas and rates are the smallest, with some scenarios even showing no significant increase trend.
- Temporal Distribution of Future Moisture Increase Rates: In the early 21st century (2021–2040) and late 21st century (2071–2100), the rate of significant SM increase is higher, while there is almost no significant increase trend in the mid-21st century (2041–2070). Additionally, the moisture increase rate in the early 21st century is generally higher than that in the late 21st century.

Supplementary Materials: The following supporting information can be downloaded at https://www.mdpi.com/article/10.3390/rs16234367/s1. Table S1; Figures S1–S20.

Author Contributions: Conceptualization, Z.L., S.L., J.W. and X.T.; methodology, Z.L.; software, Z.L.; validation, Z.L.; formal analysis, Z.L.; investigation, Z.L., S.L., J.W. and X.T.; resources, S.L.; data curation, Z.L.; writing—original draft preparation, Z.L. and S.L.; writing—review and editing, Z.L. and S.L.; visualization, Z.L.; supervision, S.L.; project administration, S.L.; funding acquisition, S.L. All authors have read and agreed to the published version of the manuscript.

Funding: This work was supported jointly by the National Natural Science Foundation of China (U20A2081), West Light Foundation of the Chinese Academy of Sciences (xbzg-zdsys-202102), and the program of the Key Laboratory of Cryospheric Science and Frozen Soil Engineering,CAS (CSFSE-ZZ-2410).

Data Availability Statement: The $CMIP6_{UNet\text{-}Gan}$ data can be downloaded from the following link: https://figshare.com/articles/dataset/UNet-Gan_based_soil_moisture_data_of_Three_River_Source_Region_in_history_and_four_future_emission_scenarios/26827576 (accessed on 1 August 2024).Our code is open-sourced at https://github.com/lizhuoq/UNet-Gan (accessed on 1 August 2024). The ERA5-Land data used in this study can be downloaded from https://cds.climate.copernicus.eu/datasets/reanalysis-era5-land-monthly-means?tab=download (accessed on 1 August 2024). The AMSMQTP data are available at http://www.ncdc.ac.cn/portal/metadata/4d94e0b3-a10c-43f6-b971-23e2df62c8ff (accessed on 1 August 2024). The CMIP6 data can be accessed via https://cds.climate.copernicus.eu/datasets/projections-cmip6?tab=download (accessed on 1 August 2024), and the ISMN data are available for download at https://ismn.earth/en/ (accessed on 1 August 2024).

Acknowledgments: This study utilized the code from the pyMannKendall repository (https://github.com/mmhs013/pyMannKendall, accessed on 1 August 2024) for the Mann-Kendall trend analysis. We thank the contributors to this repository for their efforts.

Conflicts of Interest: The authors declare no conflict of interest.

References

1. Rodriguez-Iturbe, I.; D'odorico, P.; Porporato, A.; Ridolfi, L. On the spatial and temporal links between vegetation, climate, and soil moisture. *Water Resour. Res.* **1999**, *35*, 3709–3722. [CrossRef]
2. Wasko, C.; Nathan, R.; Peel, M.C. Changes in antecedent soil moisture modulate flood seasonality in a changing climate. *Water Resour. Res.* **2020**, *56*, e2019WR026300. [CrossRef]
3. Humphrey, V.; Berg, A.; Ciais, P.; Gentine, P.; Jung, M.; Reichstein, M.; Seneviratne, S.I.; Frankenberg, C. Soil moisture–atmosphere feedback dominates land carbon uptake variability. *Nature* **2021**, *592*, 65–69. [CrossRef] [PubMed]
4. Wu, D.; Wang, T.; Di, C.; Wang, L.; Chen, X. Investigation of controls on the regional soil moisture spatiotemporal patterns across different climate zones. *Sci. Total Environ.* **2020**, *726*, 138214. [CrossRef]
5. Li, W.; Migliavacca, M.; Forkel, M.; Denissen, J.M.; Reichstein, M.; Yang, H.; Duveiller, G.; Weber, U.; Orth, R. Widespread increasing vegetation sensitivity to soil moisture. *Nat. Commun.* **2022**, *13*, 3959. [CrossRef]
6. Tan, X.; Luo, S.; Li, H.; Hao, X.; Wang, J.; Dong, Q.; Chen, Z. Investigating the effects of snow cover and vegetation on soil temperature using remote sensing indicators in the three river source region, China. *Remote Sens.* **2022**, *14*, 4114. [CrossRef]
7. Luo, S.; Wang, J.; Tan, X.; Meng, X.; Shang, L.; Li, H.; Zhou, B.; Chen, Q. Characteristics of ground surface heat flux for alpine vegetation in freeze-thaw cycles in the three river source region. *Renew. Energy* **2024**, *221*, 119793. [CrossRef]
8. Liang, L.; Li, L.; Liu, C.; Cuo, L. Climate change in the Tibetan Plateau Three Rivers Source Region: 1960–2009. *Int. J. Climatol.* **2013**, *33*, 2900–2916. [CrossRef]
9. Li, H.; Yan, L.; Wen, T.; Feng, X. Characteristics of Climate Change and Its Impact Assessment in the Three-River Regions. *Plateau Meteorol.* **2022**, *41*, 306–316.
10. Luo, S.; Fang, X.; Lyu, S.; Jiang, Q.; Wang, J. Interdecadal changes in the freeze depth and period of frozen soil on the Three Rivers Source Region in China from 1960 to 2014. *Adv. Meteorol.* **2017**, *2017*, 5931467. [CrossRef]
11. Fang, X.; Luo, S.; Lyu, S.; Cheng, C.; Li, Z.; Zhang, S. Numerical modeling of the responses of soil temperature and soil moisture to climate change over the Tibetan Plateau, 1961–2010. *Int. J. Climatol.* **2021**, *41*, 4134–4150. [CrossRef]
12. O'Neill, B.C.; Tebaldi, C.; Van Vuuren, D.P.; Eyring, V.; Friedlingstein, P.; Hurtt, G.; Knutti, R.; Kriegler, E.; Lamarque, J.F.; Lowe, J.; et al. The scenario model intercomparison project (ScenarioMIP) for CMIP6. *Geosci. Model Dev.* **2016**, *9*, 3461–3482. [CrossRef]
13. Zelinka, M.D.; Myers, T.A.; McCoy, D.T.; Po-Chedley, S.; Caldwell, P.M.; Ceppi, P.; Klein, S.A.; Taylor, K.E. Causes of higher climate sensitivity in CMIP6 models. *Geophys. Res. Lett.* **2020**, *47*, e2019GL085782. [CrossRef]
14. Tebaldi, C.; Debeire, K.; Eyring, V.; Fischer, E.; Fyfe, J.; Friedlingstein, P.; Knutti, R.; Lowe, J.; O'Neill, B.; Sanderson, B.; et al. Climate model projections from the scenario model intercomparison project (ScenarioMIP) of CMIP6. *Earth Syst. Dyn.* **2021**, *12*, 253–293. [CrossRef]
15. Cook, B.I.; Mankin, J.S.; Marvel, K.; Williams, A.P.; Smerdon, J.E.; Anchukaitis, K.J. Twenty-first century drought projections in the CMIP6 forcing scenarios. *Earth's Future* **2020**, *8*, e2019EF001461. [CrossRef]
16. Hirsch, A.L.; Ridder, N.N.; Perkins-Kirkpatrick, S.E.; Ukkola, A. CMIP6 MultiModel evaluation of present-day heatwave attributes. *Geophys. Res. Lett.* **2021**, *48*, e2021GL095161. [CrossRef]
17. Gebrechorkos, S.; Leyland, J.; Slater, L.; Wortmann, M.; Ashworth, P.J.; Bennett, G.L.; Boothroyd, R.; Cloke, H.; Delorme, P.; Griffith, H.; et al. A high-resolution daily global dataset of statistically downscaled CMIP6 models for climate impact analyses. *Sci. Data* **2023**, *10*, 611. [CrossRef]
18. Kreienkamp, F.; Lorenz, P.; Geiger, T. Statistically downscaled CMIP6 projections show stronger warming for Germany. *Atmosphere* **2020**, *11*, 1245. [CrossRef]
19. Tian, J.; Zhang, Z.; Ahmed, Z.; Zhang, L.; Su, B.; Tao, H.; Jiang, T. Projections of precipitation over China based on CMIP6 models. *Stoch. Environ. Res. Risk Assess.* **2021**, *35*, 831–848. [CrossRef]
20. Noël, T.; Loukos, H.; Defrance, D.; Vrac, M.; Levavasseur, G. Extending the global high-resolution downscaled projections dataset to include CMIP6 projections at increased resolution coherent with the ERA5-Land reanalysis. *Data Brief* **2022**, *45*, 108669. [CrossRef]
21. Dey, A.; Sahoo, D.P.; Kumar, R.; Remesan, R. A multimodel ensemble machine learning approach for CMIP6 climate model projections in an Indian River basin. *Int. J. Climatol.* **2022**, *42*, 9215–9236. [CrossRef]
22. Feng, D.; Wang, G.; Wei, X.; Amankwah, S.O.Y.; Hu, Y.; Luo, Z.; Hagan, D.F.T.; Ullah, W. Merging and downscaling soil moisture data from CMIP6 projections using deep learning method. *Front. Environ. Sci.* **2022**, *10*, 847475. [CrossRef]
23. Soltani, K.; Amiri, A.; Ebtehaj, I.; Cheshmehghasabani, H.; Fazeli, S.; Gumiere, S.J.; Bonakdari, H. Advanced Forecasting of Drought Zones in Canada Using Deep Learning and CMIP6 Projections. *Climate* **2024**, *12*, 119. [CrossRef]
24. Goodfellow, I.; Pouget-Abadie, J.; Mirza, M.; Xu, B.; Warde-Farley, D.; Ozair, S.; Courville, A.; Bengio, Y. Generative adversarial networks. *Commun. ACM* **2020**, *63*, 139–144. [CrossRef]

25. Creswell, A.; White, T.; Dumoulin, V.; Arulkumaran, K.; Sengupta, B.; Bharath, A.A. Generative adversarial networks: An overview. *IEEE Signal Process. Mag.* **2018**, *35*, 53–65. [CrossRef]
26. Wang, K.; Gou, C.; Duan, Y.; Lin, Y.; Zheng, X.; Wang, F.Y. Generative adversarial networks: Introduction and outlook. *IEEE/CAA J. Autom. Sin.* **2017**, *4*, 588–598. [CrossRef]
27. Jozdani, S.; Chen, D.; Pouliot, D.; Johnson, B.A. A review and meta-analysis of generative adversarial networks and their applications in remote sensing. *Int. J. Appl. Earth Obs. Geoinf.* **2022**, *108*, 102734. [CrossRef]
28. Zhang, H.; Song, Y.; Han, C.; Zhang, L. Remote sensing image spatiotemporal fusion using a generative adversarial network. *IEEE Trans. Geosci. Remote Sens.* **2020**, *59*, 4273–4286. [CrossRef]
29. Ronneberger, O.; Fischer, P.; Brox, T. U-Net: Convolutional networks for biomedical image segmentation. In *Medical Image Computing and Computer-Assisted Intervention—MICCAI 2015, Proceedings of the 18th International Conference, Munich, Germany, 5–9 October 2015*; Proceedings, Part III 18; Springer: Cham, Switzerland, 2015; pp. 234–241.
30. Luo, S.; Fang, X.; Lyu, S.; Ma, D.; Chang, Y.; Song, M.; Chen, H. Frozen ground temperature trends associated with climate change in the Tibetan Plateau Three River Source Region from 1980 to 2014. *Clim. Res.* **2016**, *67*, 241–255. [CrossRef]
31. Goodman, D.S. Qinghai and the emergence of the West: Nationalities, communal interaction and national integration. *China Q.* **2004**, *178*, 379–399. [CrossRef]
32. Yeh, E.T. Green governmentality and pastoralism in western China: 'Converting pastures to grasslands'. *Nomadic Peoples* **2005**, *9*, 9–30. [CrossRef]
33. Muñoz-Sabater, J.; Dutra, E.; Agustí-Panareda, A.; Albergel, C.; Arduini, G.; Balsamo, G.; Boussetta, S.; Choulga, M.; Harrigan, S.; Hersbach, H.; et al. ERA5-Land: A state-of-the-art global reanalysis dataset for land applications. *Earth Syst. Sci. Data* **2021**, *13*, 4349–4383. [CrossRef]
34. Wang, Y.R.; Hessen, D.O.; Samset, B.H.; Stordal, F. Evaluating global and regional land warming trends in the past decades with both MODIS and ERA5-Land land surface temperature data. *Remote Sens. Environ.* **2022**, *280*, 113181. [CrossRef]
35. Gomis-Cebolla, J.; Rattayova, V.; Salazar-Galán, S.; Francés, F. Evaluation of ERA5 and ERA5-Land reanalysis precipitation datasets over Spain (1951–2020). *Atmos. Res.* **2023**, *284*, 106606. [CrossRef]
36. Luo, S.; Li, Z.; Tan, X.; Hao, X. *The Dataset of Daily Soil Moisture at 0.1-Degree Resolution over Five Layers on the Qinghai–Tibet Plateau from 2000 to 2021*; National Cryosphere Desert Data Center: Lanzhou, China, 2024. [CrossRef]
37. Turnock, S.T.; Allen, R.J.; Andrews, M.; Bauer, S.E.; Deushi, M.; Emmons, L.; Good, P.; Horowitz, L.; John, J.G.; Michou, M.; et al. Historical and future changes in air pollutants from CMIP6 models. *Atmos. Chem. Phys.* **2020**, *20*, 14547–14579. [CrossRef]
38. Su, B.; Huang, J.; Mondal, S.K.; Zhai, J.; Wang, Y.; Wen, S.; Gao, M.; Lv, Y.; Jiang, S.; Jiang, T.; et al. Insight from CMIP6 SSP-RCP scenarios for future drought characteristics in China. *Atmos. Res.* **2021**, *250*, 105375. [CrossRef]
39. Olén, N.B.; Lehsten, V. High-resolution global population projections dataset developed with CMIP6 RCP and SSP scenarios for year 2010–2100. *Data Brief* **2022**, *40*, 107804. [CrossRef]
40. Dorigo, W.; Himmelbauer, I.; Aberer, D.; Schremmer, L.; Petrakovic, I.; Zappa, L.; Preimesberger, W.; Xaver, A.; Annor, F.; Ardö, J.; et al. The International Soil Moisture Network: Serving Earth system science for over a decade. *Hydrol. Earth Syst. Sci.* **2021**, *25*, 5749–5804. [CrossRef]
41. Dorigo, W.; Xaver, A.; Vreugdenhil, M.; Gruber, A.; Dostálová, A.; Sanchis-Dufau, A.D.; Zamojski, D.; Cordes, C.; Wagner, W.; Drusch, M. Global Automated Quality Control of In Situ Soil Moisture Data from the International Soil Moisture Network. *Vadose Zone J.* **2013**, *12*, vzj2012.0097. [CrossRef]
42. Yang, K.; Qin, J.; Zhao, L.; Chen, Y.; Tang, W.; Han, M.; Zhu, l.; Chen, Z.; Lv, N.; Ding, B.; et al. A Multi-Scale Soil Moisture and Freeze-Thaw Monitoring Network on the Third Pole. *Bull. Am. Meteorol. Soc.* **2013**, *94*, 1907–1916. [CrossRef]
43. Dente, L.; Su, Z.; Wen, J. Validation of SMOS soil moisture products over the Maqu and Twente regions. *Sensors* **2012**, *12*, 9965–9986. [CrossRef] [PubMed]
44. Su, Z.; Wen, J.; Dente, L.; Velde, R.; Wang, L.; Ma, Y.; Yang, K.; Hu, Z. The Tibetan Plateau observatory of plateau scale soil moisture and soil temperature (Tibet-Obs) for quantifying uncertainties in coarse resolution satellite and model products. *Hydrol. Earth Syst. Sci.* **2011**, *15*, 2303–2316. [CrossRef]
45. Hussain, M.; Mahmud, I. pyMannKendall: A python package for non parametric Mann Kendall family of trend tests. *J. Open Source Softw.* **2019**, *4*, 1556. [CrossRef]
46. Huang, H.; Lin, L.; Tong, R.; Hu, H.; Zhang, Q.; Iwamoto, Y.; Han, X.; Chen, Y.W.; Wu, J. Unet 3+: A full-scale connected unet for medical image segmentation. In Proceedings of the ICASSP 2020—2020 IEEE International Conference on Acoustics, Speech and Signal Processing (ICASSP), Barcelona, Spain, 4–8 May 2020; pp. 1055–1059.
47. Li, Z.; Liu, F.; Yang, W.; Peng, S.; Zhou, J. A survey of convolutional neural networks: Analysis, applications, and prospects. *IEEE Trans. Neural Netw. Learn. Syst.* **2021**, *33*, 6999–7019. [CrossRef] [PubMed]
48. Ledig, C.; Theis, L.; Huszár, F.; Caballero, J.; Cunningham, A.; Acosta, A.; Aitken, A.; Tejani, A.; Totz, J.; Wang, Z.; et al. Photo-realistic single image super-resolution using a generative adversarial network. In Proceedings of the IEEE Conference on Computer Vision and Pattern Recognition, Honolulu, HI, USA, 21–26 July 2017; pp. 4681–4690.
49. Wang, X.; Yu, K.; Wu, S.; Gu, J.; Liu, Y.; Dong, C.; Qiao, Y.; Change Loy, C. Esrgan: Enhanced super-resolution generative adversarial networks. In Proceedings of the European Conference on Computer Vision (ECCV) Workshops, Munich, Germany, 8–14 September 2018.
50. Breiman, L. Random forests. *Mach. Learn.* **2001**, *45*, 5–32. [CrossRef]

51. Paszke, A.; Gross, S.; Massa, F.; Lerer, A.; Bradbury, J.; Chanan, G.; Killeen, T.; Lin, Z.; Gimelshein, N.; Antiga, L.; et al. Pytorch: An imperative style, high-performance deep learning library. *Adv. Neural Inf. Process. Syst.* **2019**, *32*.
52. Dong, J.; Ochsner, T.E. Soil texture often exerts a stronger influence than precipitation on mesoscale soil moisture patterns. *Water Resour. Res.* **2018**, *54*, 2199–2211. [CrossRef]
53. Ran, Q.; Wang, F.; Gao, J. The effect of storm movement on infiltration, runoff and soil erosion in a semi-arid catchment. *Hydrol. Process.* **2020**, *34*, 4526–4540. [CrossRef]
54. Zhou, S.; Williams, A.P.; Lintner, B.R.; Berg, A.M.; Zhang, Y.; Keenan, T.F.; Cook, B.I.; Hagemann, S.; Seneviratne, S.I.; Gentine, P. Soil moisture–atmosphere feedbacks mitigate declining water availability in drylands. *Nat. Clim. Chang.* **2021**, *11*, 38–44. [CrossRef]
55. Xu, M.; Hou, Z.; Kang, S.; Wu, X.; Han, H.; Wang, P. Projection of snowfall and precipitation phase changes over the Northwest China based on CMIP6 multimodels. *J. Hydrol.* **2024**, *641*, 131743. [CrossRef]
56. Zhang, J.; Wu, T.; Xin, X.; Lu, Y.; Yan, J.; Zhang, F.; Liu, L.; Zhao, H. Surface air temperature trend over the Tibetan Plateau in CMIP6 and its constraint in future projection. *J. Geophys. Res. Atmos.* **2023**, *128*, e2023JD039527. [CrossRef]
57. Cui, Y.; Zeng, C.; Zhou, J.; Xie, H.; Wan, W.; Hu, L.; Xiong, W.; Chen, X.; Fan, W.; Hong, Y. A spatio-temporal continuous soil moisture dataset over the Tibet Plateau from 2002 to 2015. *Sci. Data* **2019**, *6*, 247. [CrossRef] [PubMed]
58. Brocca, L.; Zhao, W.; Lu, H. High-resolution observations from space to address new applications in hydrology. *Innovation* **2023**, *4*, 100437. [CrossRef] [PubMed]